Government of **Western Australia**
Department of **Mines and Petroleum**

RECORD 2010/12

IN SITU U–PB MONAZITE AND XENOTIME GEOCHRONOLOGY OF THE ABRA POLYMETALLIC DEPOSIT AND ASSOCIATED SEDIMENTARY AND VOLCANIC ROCKS, BANGEMALL SUPERGROUP, WESTERN AUSTRALIA

by
B Rasmussen, IR Fletcher, JR Muhling, C Gregory, AM Thorne, HN Cutten, F Pirajno, and A Hell

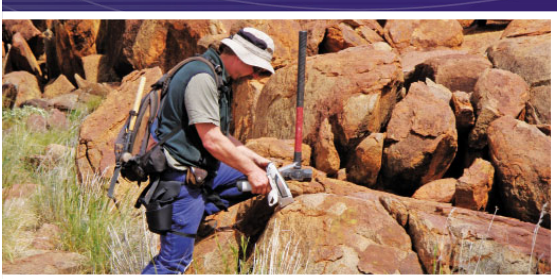

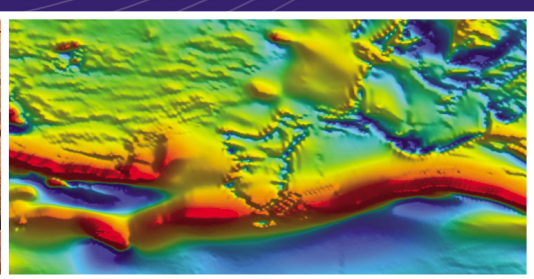

Geological Survey of
Western Australia

Government of Western Australia
Department of Mines and Petroleum

Record 2010/12

IN SITU U–PB MONAZITE AND XENOTIME GEOCHRONOLOGY OF THE ABRA POLYMETALLIC DEPOSIT AND ASSOCIATED SEDIMENTARY AND VOLCANIC ROCKS, BANGEMALL SUPERGROUP, WESTERN AUSTRALIA

by
B Rasmussen[1], IR Fletcher[1], JR Muhling[2], C Gregory[1], AM Thorne[3], HN Cutten[3], F Pirajno[3], and A Hell[4]

[1] Department of Applied Geology, Curtin University, GPO Box U1987, Perth WA 6845
[2] Centre for Microscopy, Characterisation and Analysis, The University of Western Australia, 35 Stirling Highway, Crawley WA 6009
[3] Geological Survey of Western Australia, Mineral House, 100 Plain Street, East Perth WA 6004
[4] Abra Mining Limited, Level 1, 34 Colin Street, West Perth WA 6005

Geological Survey of Western Australia

John de Laeter Centre
Isotope Research for the Earth and Environment

MINISTER FOR MINES AND PETROLEUM
Hon. Norman Moore MLC

DIRECTOR GENERAL, DEPARTMENT OF MINES AND PETROLEUM
Richard Sellers

ACTING EXECUTIVE DIRECTOR, GEOLOGICAL SURVEY OF WESTERN AUSTRALIA
Rick Rogerson

REFERENCE
The recommended reference for this publication is:
Rasmussen, B, Fletcher, IR, Muhling, JR, Gregory, C, Thorne, AM, Cutten, HN, Pirajno, F and Hell, A 2010, In situ U–Pb monazite and xenotime geochronology of the Abra polymetallic deposit and associated sedimentary and volcanic rocks, Bangemall Supergroup, Western Australia: Geological Survey of Western Australia, Record 2010/12, 31p.

National Library of Australia Card Number and ISBN 978-1-74168-304-2

Grid references in this publication refer to the Geocentric Datum of Australia 1994 (GDA94). Locations mentioned in the text are referenced using Map Grid Australia (MGA) coordinates, Zone 50. All locations are quoted to at least the nearest 100 m.

Published 2010 by Geological Survey of Western Australia
This Record is published in digital format (PDF) and is available online at www.dmp.wa.gov.au/GSWApublications.
Laser-printed copies can be ordered from the Information Centre for the cost of printing and binding.

Further details of geological publications and maps produced by the Geological Survey of Western Australia are available from:
Information Centre
Department of Mines and Petroleum
100 Plain Street
EAST PERTH, WESTERN AUSTRALIA 6004
Telephone: +61 8 9222 3459 Facsimile: +61 8 9222 3444
www.dmp.wa.gov.au/GSWApublications

Contents

Abstract 1
Introduction 2
Geological setting 2
Gascoyne Province 2
Edmund Basin 4
Irregully Formation 4
Kiangi Creek Formation 6
Tangadee Rhyolite 6
Coherent rhyolite 6
Felsic volcaniclastic rocks 7
Evidence for syndepositional emplacement 7
Discovery, Devil Creek, and Ullawarra Formations 9
Collier Basin 9
Paleoproterozoic to Neoproterozoic tectonothermal history of the Capricorn Orogen 9
1620–1465 Ma Edmund Basin and Narimbunna Dolerite 9
Collier Basin and 1280–1250 Ma event 9
1078–1070 Ma Warakurna event 9
1030–950 Ma Edmundian Orogeny 10
900–820 Ma event 10
c. 570 Ma Mulka Tectonic Event 10
Mineralization 10
Samples 11
Analytical methods 12
Results 12
Petrography 12
Abra deposit 12
Tangadee Rhyolite 15
SHRIMP geochronology 15
Zircon 15
Kiangi Creek sandstone hosting Abra mineralization (GSWA 149084, 149087) 15
Xenotime 15
Kiangi Creek Formation sandstone, occurring within or above the Abra mineralization (GSWA 149085, 149088, 149089, 149090, 149093) 20
Tangadee Rhyolite (GSWA 149020) 20
Monazite 24
Inclusions in detrital quartz (GSWA 149085, 149088, 149089, 149090) 24
Hydrothermal monazite (GSWA149085, 149086, 149093) 24
Discussion 24
Abra mineralization (c. 1385 Ma) 28
c. 1385 Ma events in the Capricorn Orogen 28
Tangadee Rhyolite (c. 1235 Ma and c. 1030 Ma) 28
c. 1235 and c. 1040 Ma events in the Capricorn Orogen 29
Conclusions 29
Acknowledgements 29
References 30

Figures

1. Simplified geological map of the Capricorn Orogen showing the location of the Abra polymetallic deposit and the geological sketch map shown in Figure 2 2
2. Interpreted bedrock geology of the area showing the location of Abra in relation to the major structures and depositional facies of the Kiangi Creek Formation 2
3. Field photograph showing weakly to strongly foliated, porphyritic, coarse-grained granodiorite, with locally abundant K-feldspar phenocrysts (Moorarie Supersuite) 4
4. Summary of Bangemall Supergroup stratigraphy with the location of the Kiangi Creek Formation highlighted 5
5. Correlation of the stratigraphic units proposed by Vogt (1995) for the Abra district with the regional stratigraphy of GSWA 5
6. Field photographs of Tangadee Rhyolite 7
7. Schematic representation of Abra host-rock stratigraphy and sample locations 12
8. Plane polarized light images of detrital quartz grains 13

9. Back-scattered electron images of K-feldspar in the sandstone (sample 149084) hosting the Abra mineralization 14
10. Back-scattered electron images 16
11. Back-scattered electron images of monazite 17
12. Heavy mineral separates from GSWA mount G08-3 (sample 149020) 18
13. Concordia plot of the U–Pb data for Abra xenotimes exposed in thin sections 22
14. Concordia plot of the U–Pb data for Tangadee Rhyolite xenotime 22
15. Probability density diagram of $^{207}Pb/^{206}Pb$ dates for the two principal groups of xenotime data from Tangadee Rhyolite 22
16. Probability density diagram of $^{207}Pb/^{206}Pb$ dates for Abra monazite inclusions 27
17. Concordia plot of the U–Pb data for Abra hydrothermal monazite with <1% common ^{206}Pb 27
18. Pb/Pb (inverse) isochron plot for Abra hydrothermal monazite 27

Tables

1. Chemical analyses of the Tangadee Rhyolite 8
2. Locations of samples used in this study 11
3. SHRIMP U–Pb data for zircon from Abra sandstones and the Tangadee Rhyolite 19
4. SHRIMP U–Pb data for Abra xenotime 21
5. SHRIMP U–Pb data for Tangadee Rhyolite xenotime 23
6. SHRIMP U–Pb data for Abra monazite inclusions 25
7. SHRIMP U–Pb data for Abra hydrothermal monazite 26

In situ U–Pb monazite and xenotime geochronology of the Abra polymetallic deposit and associated sedimentary and volcanic rocks, Bangemall Supergroup, Western Australia

by

B Rasmussen[1], IR Fletcher[1], JR Muhling[2], C Gregory[1], AM Thorne[3], HN Cutten[3], F Pirajno[3], and AHell[4]

Abstract

Abra is a major lead–silver–copper–gold deposit within the Bangemall Supergroup that has a total indicated and inferred resource estimate of 93 million tonnes at 4.0% lead and 10 g/t silver and 14 million tonnes at 0.6% copper and 0.5 g/t gold. The mineralization lies within the upper part of the locally defined Gap Well Formation, and in the lower part of the overlying West Creek Formation. These units correlate respectively with the Irregully and lower Kiangi Creek Formations of the Edmund Group.

The Abra deposit is characterized by a funnel-shaped brecciated zone, interpreted as a breccia feeder-pipe, overlain by stratabound mineralization made up of the Red Zone, an underlying Black Zone, and a stringer (feeder) zone. The Red Zone is characterized by banded jaspilite, hematite, galena, pyrite, quartz, abundant barite, and siderite. The Black Zone consists of veins and rhythmically banded Pb, Zn, and minor Cu sulfides, laminated and/or brecciated hematite, magnetite, Fe-rich carbonate, barite, and scheelite.

In situ Sensitive high-resolution ion microprobe (SHRIMP) U–Pb geochronology of detrital zircon, monazite, and xenotime in sandstones from the Abra deposit yields a range of dates from c. 2450 Ma to c. 1675 Ma, consistent with results from previous detrital zircon studies. SHRIMP dating of hydrothermal monazite from the Abra deposit suggests that a mineralization event occurred at c. 1385 Ma. The presence of c. 1465 Ma metamorphic/hydrothermal monazite in sandstones from Abra indicates that the host rocks are older and therefore belong to the Edmund Group. SHRIMP geochronology of xenotime extracted from the Tangadee Rhyolite, which outcrops within the lower Kiangi Creek Formation close to the Abra deposit, yields two main age components corresponding to oscillatory-zoned cores and unzoned rims. The cores are interpreted as magmatic in origin and indicate a possible eruption age of c. 1235 Ma, whereas the rims are interpreted to record a later hydrothermal event at c. 1030 Ma. If this interpretation is correct, then the sedimentary succession containing the rhyolite is younger than the Edmund Group (<1640 Ma and >1465 Ma), and may belong to the basal Collier Group (<1465 Ma and >1070 Ma) although the geological setting does not support this.

KEYWORDS: Bangemall Supergroup, Edmund Group, Collier Group, Capricorn Orogen, Edmund Basin, Collier Basin, base metals, gold, mineralization, Abra deposit, geochronology, rock geochemistry, Sensitive high-resolution ion microprobe, SHRIMP geochronology.

[1] Department of Applied Geology, Curtin University, GPO Box U1987, Perth WA 6845
[2] Centre for Microscopy, Characterisation and Analysis, The University of Western Australia, 35 Stirling Highway, Crawley WA 6009
[3] Geological Survey of Western Australia, Mineral House, 100 Plain Street, East Perth WA 6004
[4] Abra Mining Limited, Level 1, 34 Colin Street, West Perth WA 6005

Introduction

Abra is a major lead–silver–copper–gold deposit within the Bangemall Supergroup that has a total indicated and inferred resource estimate of 93 million tonnes at 4.0% lead and 10 g/t silver and 14 million tonnes at 0.6% copper and 0.5 g/t gold (Abra Mining Limited, 2010). Furthermore, drilling during 2008 has confirmed that the Abra deposit remains open in most directions, supporting its status as the most significant mineral discovery in the central Capricorn Orogen to date.

The Abra mineralization occurs within the upper part of the locally defined Gap Well Formation, and in the lower part of the overlying West Creek Formation. These units correlate with the Irregully and Kiangi Creek Formations (depositional packages 1 and 3) respectively of the Edmund Group, the lowermost stratigraphic unit within the Bangemall Supergroup. Mineralization does not outcrop, the uppermost part of the ore body being 280 m below ground level.

The Bangemall Supergroup, comprising the Edmund and Collier Groups, was deposited in the Edmund and Collier Basins respectively, in response to intracratonic extensional reactivation of the Paleoproterozoic Capricorn Orogen between 1620 Ma and 1070 Ma. The supergroup can be further divided into six depositional packages bounded by unconformities or major marine flooding surfaces (Martin and Thorne, 2004). Detrital zircon geochronology and zircon/baddeleyite geochronology of crosscutting dolerite sills has produced only loose constraints on the age of the Edmund Group of c. 1620–1465 Ma and c. 1465–1070 Ma for the overlying Collier Group (Martin and Thorne, 2004).

Previous attempts to determine the age of the Abra host rocks and mineralization have been unsuccessful. Gee et al. (1976) obtained a Rb–Sr date of 1098 ± 42 Ma from the Tangadee Rhyolite that outcrops within the host stratigraphy 10 to 25 km east of the Abra deposit. However, this age is considerably less than the younger age limit for the Edmund Group at 1465 Ma. The Tangadee Rhyolite subsequently yielded a SHRIMP (Sensitive high-resolution ion microprobe) U–Pb maximum age of 1638 ± 14 Ma, based on the presence of two xenocrystic zircons (Nelson, 1995a). This result is close to the Pb model age of about 1.64 Ga for galena from the Abra deposit (JR Richards, pers. comm., quoted in Collins and McDonald, 1994), but is older than the 1620 Ma maximum age for the Edmund Group (Martin et al., 2005).

An alternative approach to determine the age of the Abra deposit and its host rocks is to date the very low- to moderate-temperature events, namely deposition, early diagenesis, and mineralization through the use of monazite and xenotime. Both these minerals are versatile and powerful U–Th–Pb chronometers that can record precise ages for a variety of low-temperature (<100°C to 550°C) geological processes (Rasmussen et al., 2001, 2005, 2007a,b; Harrison et al., 2002). Monazite and xenotime do not readily undergo diffusive Pb loss during reheating but may undergo dissolution and reprecipitation, with the ability to record multiple events in a single crystal.

This report presents the results of a pilot project that uses xenotime and monazite to determine the age of the sedimentary rocks that host the Abra polymetallic deposit. The project was carried out as part of a collaborative project between the Geological Survey of Western Australia (GSWA), Abra Mining NL, and Curtin University of Technology. During the course of the project a U–Pb monazite age was also obtained for the Abra polymetallic mineralization.

Geological setting

The Abra polymetallic deposit is located at MGA 659400E 7273600N, in the east-central Edmund Basin, about 190 km southwest of Newman (Fig. 1). It is at the eastern end of the Jillawarra sub-basin (Vogt, 1995), within a structural corridor close to the junction of two major faults, the northeast-trending Bujundunna Fault and the easterly trending Quartzite Well Fault (Fig. 2). The southern margin of the structural corridor is delineated by an unnamed east-northeasterly trending fault that marks the northern margin of the Calyie Syncline. Granitic rocks of the Gascoyne Province outcrop 19 km to the east of Abra; however, most of the surface geology is dominated by fine- to coarse-grained siliciclastic and carbonate sedimentary rocks of the Edmund Group. Minor felsic volcanic rocks (Tangadee Rhyolite) also occur within this succession. Fine- to medium-grained siliciclastic rocks of the overlying Collier Group outcrop in the Calyie Syncline to the southeast of Abra.

Gascoyne Province

Weathered granitic rocks of the 1830 to 1780 Ma Moorarie Supersuite (Occhipinti and Myers, 1999; Martin et al., 2005) are the oldest rocks in the study area and are poorly exposed 18 km east-northeast of Abra, around MGA 679626E 7274145N and MGA 679775E 7278562N (Fig. 2). Most outcrops comprise weakly to strongly foliated, porphyritic, coarse-grained granodiorite, with locally abundant K-feldspar phenocrysts up to 4 cm across (Fig. 3). The granodiorite includes rafts of strongly foliated psammite and pelite and is locally crosscut by thin fluorite veins.

Nelson (1995b) obtained a SHRIMP U–Pb zircon crystallization age of 1797 ± 8 Ma from relatively fresh granodiorite from a depth of 275.9 m in Geopeko drillhole CD-1, located near the Cadabra prospect (at MGA 672610E 7275341N). The sample is coarse grained,

Figure 1. (Top right) Simplified geological map of the Capricorn Orogen showing the location of the Abra polymetallic deposit (A) and the geological sketch map shown in Figure 2.

Figure 2. (Bottom right) Interpreted bedrock geology of the area showing the location of Abra in relation to the major structures and depositional facies of the Kiangi Creek Formation.

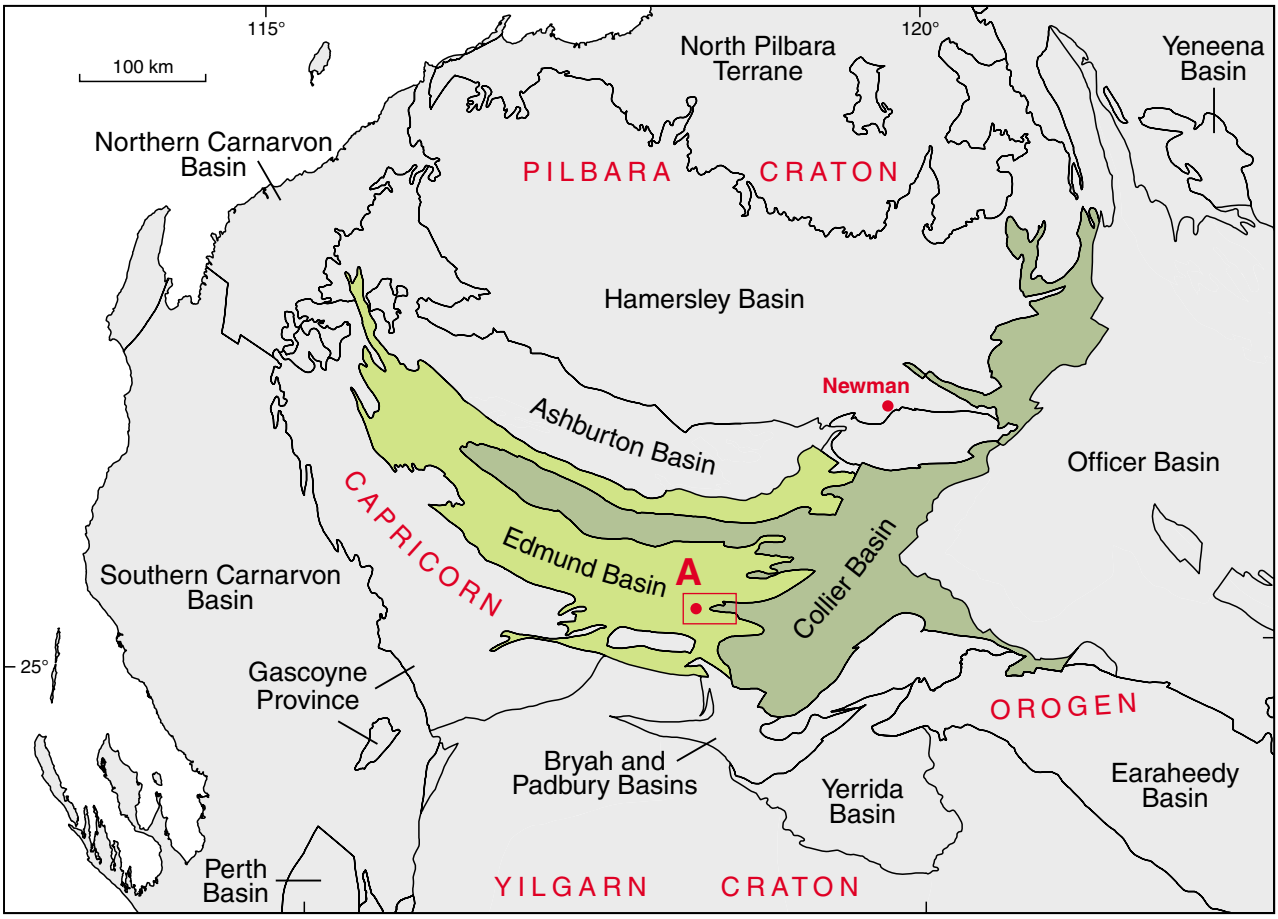
115°
120°
100 km
North Pilbara Terrane
Yeneena Basin
Northern Carnarvon Basin
PILBARA CRATON
Hamersley Basin
Newman
Ashburton Basin
Officer Basin
CAPRICORN
Edmund Basin
A
Collier Basin
Southern Carnarvon Basin
25°
Gascoyne Province
OROGEN
Bryah and Padbury Basins
Yerrida Basin
Earaheedy Basin
Perth Basin
YILGARN CRATON
AMT171
17/06/2010

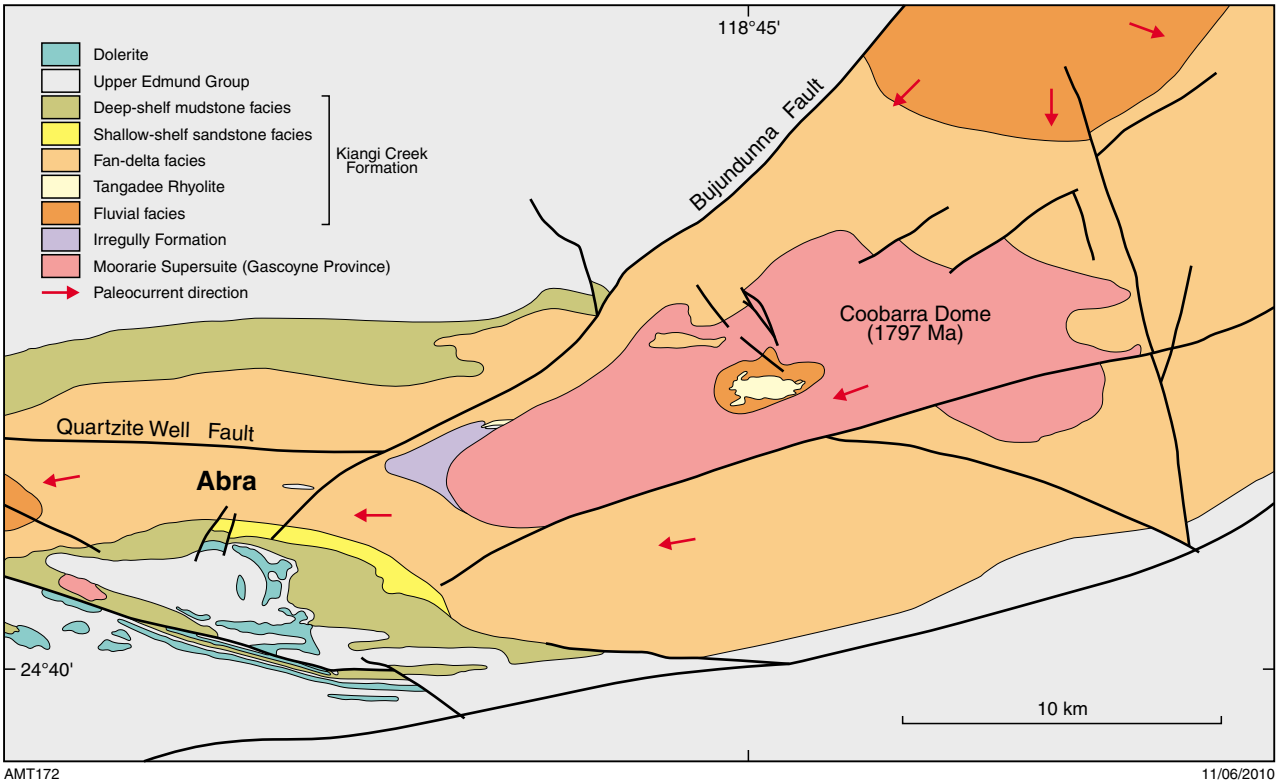
Dolerite
Upper Edmund Group
Deep-shelf mudstone facies
Shallow-shelf sandstone facies
Fan-delta facies
Tangadee Rhyolite
Fluvial facies
Kiangi Creek Formation
Irregully Formation
Moorarie Supersuite (Gascoyne Province)
Paleocurrent direction
118°45'
Bujundunna Fault
Coobarra Dome (1797 Ma)
Quartzite Well Fault
Abra
24°40'
10 km
AMT172
11/06/2010

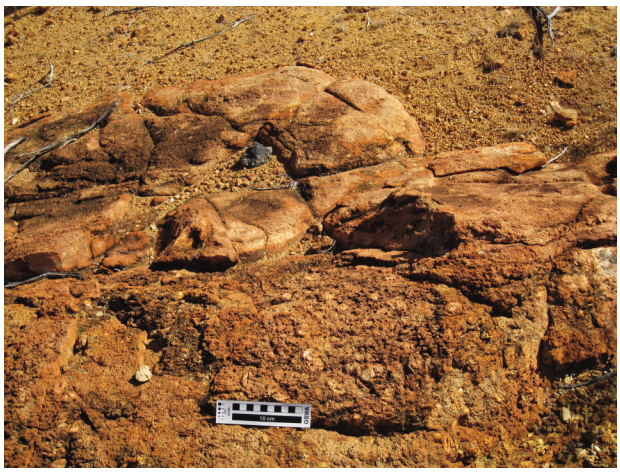

Figure 3. Field photograph showing weakly to strongly foliated, porphyritic, coarse-grained granodiorite, with locally abundant K-feldspar phenocrysts up to 4 cm across (Moorarie Supersuite).

with grains of weakly sericitized plagioclase (35–40% by volume; vol.%) up to 6 mm long, and grains of weakly perthitic feldspar (15–20 vol.%), locally with 'swapped rims' where two alkali feldspar grains are adjacent to each other. Poikilitic biotite flakes up to 5 mm long enclose feldspars, opaque oxides, and altered pyroxene. The fresh pyroxene in this rock is orthopyroxene (4 vol.% of the rock), but it is commonly altered to clay and actinolite. Pyroxene grains are commonly 0.4 to 2 mm in size, and are locally enclosed in oikocrysts of magnetite, together with apatite and zircon. The quartz, comprising 30 vol.% of the rock, is anhedral with zones of fluid inclusions and undulose extinction. Myrmekite is common between plagioclase and alkali feldspar. The alkali feldspar is mostly orthoclase with some areas of microcline twinning, with exsolution on a fine scale. Veins of chlorite and sericite are common.

Edmund Basin

The regional stratigraphy of the Edmund Group, the lowermost division of the Bangemall Supergroup is summarized in Figure 4. Within the study area the exposed succession comprises, in ascending order the Irregully Formation, Kiangi Creek Formation, Discovery Formation, Devil Creek Formation, and Ullawarra Formation. Major regional disconformities lie at the base of the Kiangi Creek Formation and the Discovery Formation (Martin and Thorne, 2004; Martin et al., 2008). The upper Kiangi Creek, Discovery, and Devil Creek Formations are intruded by dolerite sills that are correlated with the 1465 Ma Narimbunna Dolerite (Thorne and Martin, 2007), although this correlation has not yet been tested through the use of geochronology or geochemistry.

The Edmund Group is younger than 1680 to 1620 Ma granites in the underlying Gascoyne Province, and older than the c. 1465 Ma Narimbunna Dolerite that intrudes it over large areas of the Edmund Basin (Martin and Thorne, 2004). Felsic volcaniclastic rocks from the Ullawarra Formation on nearby MILGUN* have yielded a SHRIMP U–Pb zircon age of 1460 ± 9 Ma (Wingate et al., in prep.).

Irregully Formation

The Irregully Formation conformably overlies the basal Yilgatherra Formation in most of the Edmund Basin, and is conformably to unconformably overlain by either the Gooragoora Formation, Blue Billy Formation, or Kiangi Creek Formation. The principal lithologies are laminated and stromatolitic dolostone and dolorudite, and dolomitic sandstone. However, a considerable thickness of sandstone and siltstone is interbedded with the dolostone in the southern Edmund Basin (Martin and Thorne, 2000). The thickness of the Irregully Formation increases from about 350 m in the northern Edmund Basin to more than 3000 m in the southern Edmund Basin. Martin and Thorne (2004) grouped the Irregully Formation and the underlying Yilgatherra Formation into the lowest of four depositional packages that were used to interpret the major stages in the evolution of the Edmund Basin (Fig. 4).

The exposed thickness of the Irregully Formation is up to 1.2 km in the Jillawarra sub-basin and equates to units referred to as 'Gap Well Formation' by Vogt (1995; Fig. 5). Comparisons with the stratigraphy elsewhere in the southern Edmund Basin, where the Irregully Formation is at least 3 km thick, suggest that only the upper part of the Irregully Formation is exposed in the Jillawarra sub-basin.

Vogt (1995) subdivided the Gap Well (Irregully) Formation into six lithological units comprising a wide variety of mixed dolomitic and siliciclastic rocks including: dolomitic siltstone and sandstone, stromatolitic and non-stromatolitic dolostone, siltstone, and quartz sandstone. He interpreted these as shallow-water deposits, laid down in mostly low-energy, nearshore to coastal or deltaic environments.

Only the uppermost part of the Irregully Formation is exposed near Abra, the closest outcrops being around the Copper–Chert prospect, 10 km to the west of Abra (MGA 649560E 7274570N), and near Cadabra Hill, 11 km to the east of Abra (at MGA 670835E 7275544N).

Around the Copper–Chert prospect, the Irregully Formation is dominated by parallel planar to ripple cross-laminated siltstone to very fine grained sandstone, interbedded with thin, stromatolitic and non-stromatolitic dolostone, and thin- to thick-bedded quartz sandstone. Exposures of the Irregully Formation around Cadabra Hill are small, and comprise irregularly laminated dolarenite capped by brecciated jasperlitic chert.

Up to 300 m true thickness of altered and mineralized Irregully Formation are present within drillholes that penetrate into the Abra deposit (Vogt, 1995). Here the succession comprises massive to brecciated, chloritic

* Capitalized names refer to standard 1:100 000-scale map sheets, unless otherwise indicated

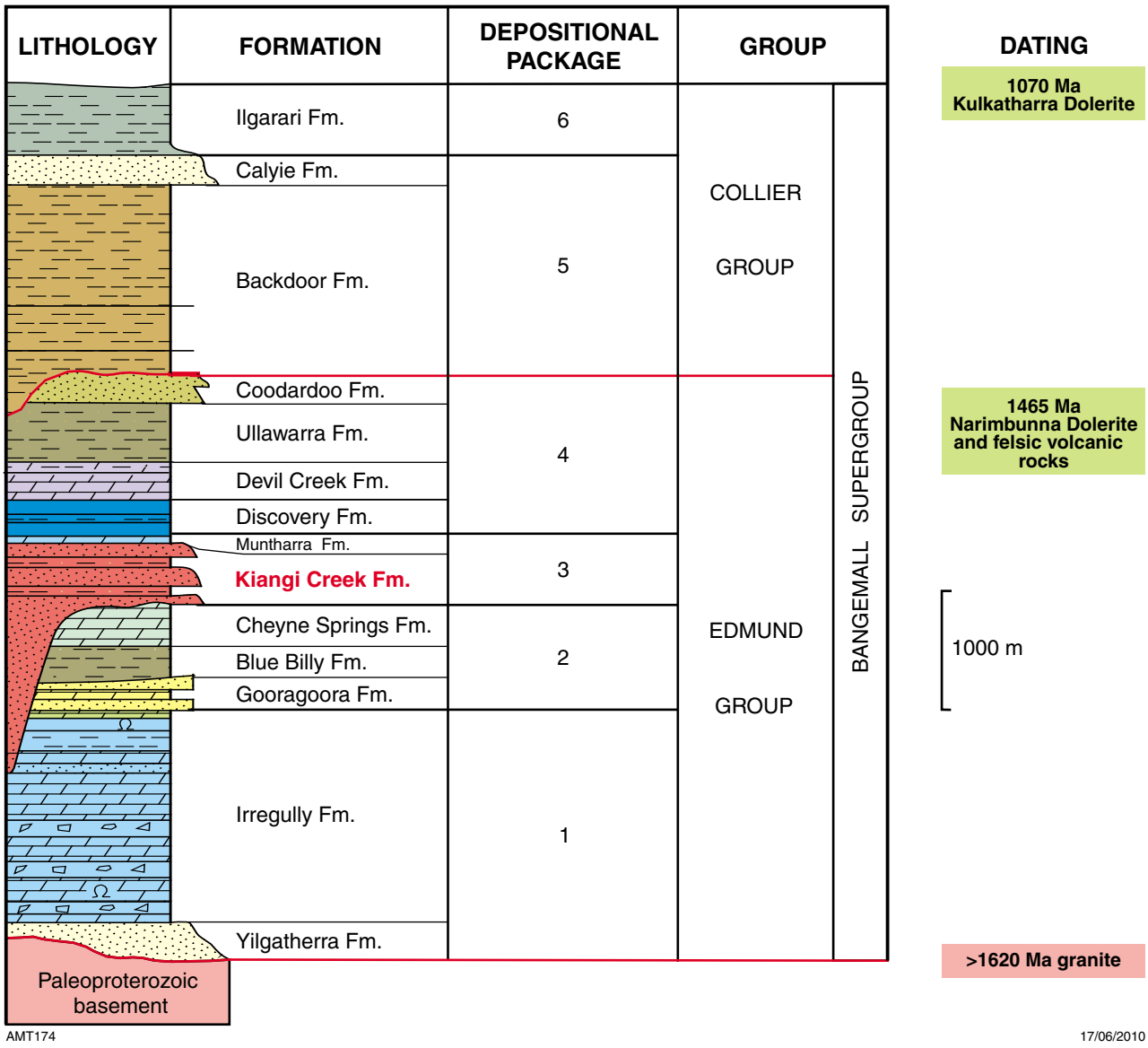

Figure 4. Summary of Bangemall Supergroup stratigraphy with the location of the Kiangi Creek Formation highlighted.

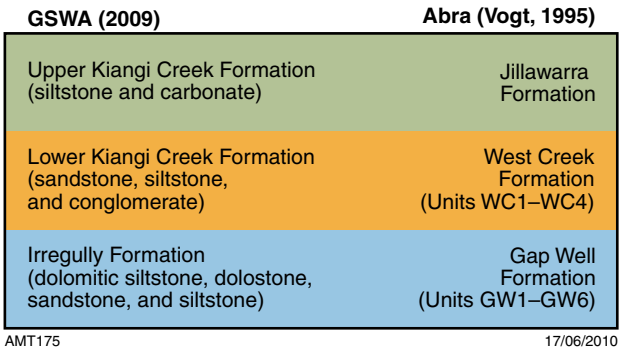

Figure 5. Correlation of the stratigraphic units proposed by Vogt (1995) for the Abra district with the regional stratigraphy of GSWA.

and silicified siltstone interbedded with fine- to medium-grained quartz sandstone.

Kiangi Creek Formation

The Kiangi Creek Formation is a 0.2 to 2.6 km thick succession of mostly fine-grained siliciclastic and carbonate sedimentary rocks that forms the middle part of the Mesoproterozoic Edmund Group. The formation is disconformable on older parts of the Edmund Group, and also rests unconformably on Gascoyne Province basement. It is conformably overlain by the locally developed Muntharra Formation or is disconformably overlain by the Discovery Formation. The Kiangi Creek Formation, together with the Muntharra Formation, make up the third of four depositional packages that Martin and Thorne (2004) used to interpret the major stages in the evolution of the Edmund Basin.

In the Jillawarra sub-basin the Kiangi Creek Formation is about 2.2 km thick and equates to rocks previously mapped as the Coobarra, Kiangi Creek, and Jillawarra Formations by Muhling and Brakel (1985) and the West Creek and Jillawarra Formations by Vogt (1995; Fig. 5). Small, lenticular bodies of rhyolite lava and thin felsic volcaniclastic units (Tangadee Rhyolite) are interbedded with the lower Kiangi Creek Formation between 6 and 17 km east of the Abra deposit (Gee et al., 1976).

Vogt (1995) subdivided the West Creek (lower Kiangi Creek) Formation into four lithostratigraphic units (WC1 to WC4) comprising, in ascending order, a lower coarse-grained sandstone and polymictic conglomerate (WC1); a thick turbiditic unit of alternating sandstone, siltstone, and minor conglomerate (WC2); a locally developed dolostone and siltstone unit (WC3); and an upper coarse-grained ferruginous sandstone with minor conglomerate (WC4). The overlying Jillawarra Formation (Muhling and Brakel, 1985) is dominated by parallel planar-laminated siltstone, interbedded with minor fine-grained sandstone and dolostone.

Thorne et al. (2009) interpreted Kiangi Creek Formation sedimentation in the Abra area as reflecting the interplay between a coarse-grained alluvial-fan system to the east and a rapidly subsiding fault-bound marine depocentre to the west. Proximal alluvial-fan sandstone and conglomerate are interbedded with the Tangadee Rhyolite, immediately southeast of the Bujundunna Fault (Muhling and Brakel, 1985) where they unconformably overlie the Moorarie Supersuite (Gascoyne Province). In this area, the most easterly outcrops record southeasterly directed paleocurrents, whereas outcrops further west indicate a southwest, then westerly paleoflow.

At Abra, alluvial-fan sandstone and conglomerate facies (equivalent to unit WC1 of Vogt, 1995) of the Kiangi Creek Formation are relatively thin (about 40 m) and disconformably overlie Irregully Formation siltstone and fine-grained sandstone. Both the Kiangi Creek Formation alluvial-fan deposits and the underlying Irregully Formation host the Abra polymetallic mineralization and associated alteration assemblage described by Collins and McDonald (1994) and Pirajno et al. (2009). The upper surface of the alluvial-fan deposits is truncated by an erosional marine-flooding surface, or ravinement, that also marks the upper limit of the most significant Abra polymetallic mineralization and alteration. This relationship suggests that the timing of Abra mineralization coincided with a period of active growth faulting, alluvial-fan sedimentation, at the start of Kiangi Creek Formation deposition. This period was also accompanied by minor felsic volcanism (see **Tangadee Rhyolite** section).

The lowermost unit of alluvial-fan sandstone and conglomerate at Abra is overlain by up to 1.3 km of fan-delta and deep marine-shelf deposits comprising siltstone interbedded with massive to normally graded, or locally cross-stratified fine- to very coarse-grained sandstone and minor conglomerate (equivalent to units WC2, WC3 of Vogt, 1995). Cross-stratified units consistently record a westwards paleoflow. These siliciclastic deposits, and locally interbedded laminated dolostone units, generally show little evidence of reworking by wave or coastal processes other than in the uppermost quartz sandstone (unit WC4 of Vogt).

The upper Kiangi Creek Formation at Abra, corresponding to the Jillawarra Formation of Muhling and Brakel (1985), is up to 0.9 km thick and records a period of decreased siliciclastic supply and expansion of the marine basin to the north and east. The stratigraphy is dominated by parallel planar-laminated mudstone and minor fine-grained sandstone, interbedded with dolomitic mudstone and planar-laminated dolostone. This unit has a sharp, apparently conformable contact with the overlying chert and silicified siltstone of the Discovery Formation.

Tangadee Rhyolite

Coherent rhyolite and lapilli-bearing felsic volcaniclastic rocks are interbedded with lower Kiangi Creek Formation sandstone and conglomerate in the area 10 to 25 km east of the Abra deposit. Gee et al. (1976), Brakel et al. (1982), and Vogt (1995) described the presence of six small rhyolite bodies that lie about 60 m above the base of the sedimentary succession, 21 km east northeast of Abra (around MGA 680550E 7276300N). In addition, Vogt (1995) recorded the presence of felsic lapilli tuff interbedded with sandstone and siltstone 11 km east northeast of Abra (MGA 671319E 7275608N). Recent GSWA mapping has shown that outcrops of thin, laminated felsic volcanic sandstone and siltstone are also present south of the Tangadee homestead road (MGA 683282E 7272144N).

Coherent rhyolite

The coherent rhyolite bodies are broadly concordant with the surrounding stratigraphy, whereas their internal structure commonly shows a fine, varicoloured lamination (Fig. 6a), with local fragmented layers (Gee et al., 1976). The rhyolite is aphanitic with a pearly lustre, and mostly colour-banded in tones of pale cream and buff. The more-oxidized varieties are pallid but the banding is accentuated by very thin pale-green and pink laminae, whereas those fresh specimens still retaining unoxidized pyrite are streaked with black and dark-grey banding. Gee et al.

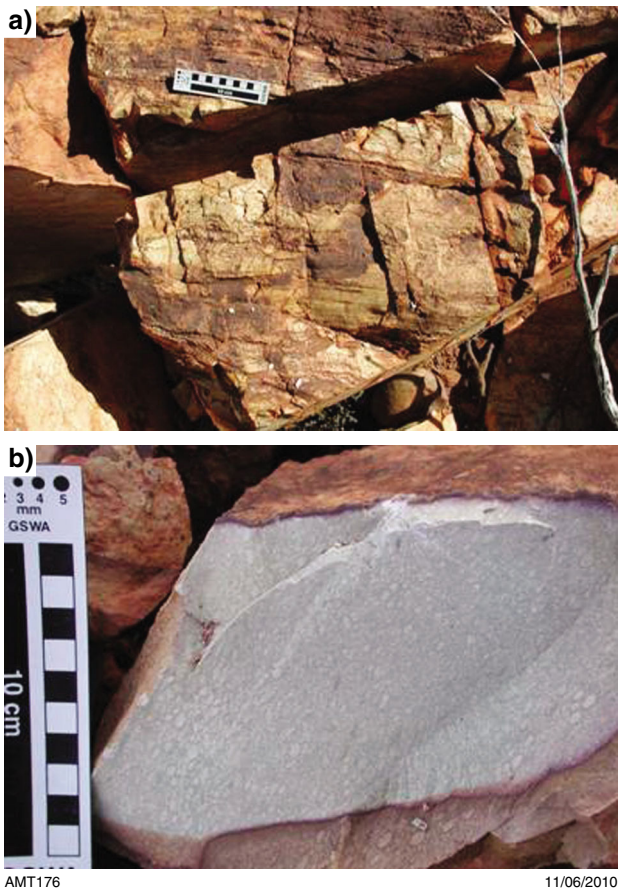

Figure 6. Field photographs of Tangadee Rhyolite: a) banded coherent facies; b) volcaniclastic facies with packed accretionary lapilli.

(1976) noted that in one rhyolite body the varicoloured layering forms a large-scale, overturned synformal fold whose upper limb is, in places, truncated and capped by a thin, planar layer of rhyolite. This folded layering is not associated with any tectonic fabric and is interpreted as primary flow banding (Gee, 1976).

In thin section the felsic rock consists mainly of euhedral to anhedral quartz and feldspar phenocrysts, in a cryptocrystalline groundmass of quartz and minor microcline, with accessory biotite, chlorite, zircon, and opaque minerals (Gee et al., 1976). The quartz phenocrysts show hexagonal or rhomboidal outlines, preserving the bipyramidal shape of ß-quartz. Most phenocrysts are embayed, indicating resorption or corrosion by the groundmass, and many have become well rounded. The feldspar phenocrysts consist of a granular intergrowth of quartz and microcline, and were considered by Gee et al. (1976) to have originally been sanidine. These authors also reported rare, irregular or distinctly spherical-shaped lithophysae of pyrite, ilmenorutile, chlorite, and carbonate encased by quartz and microcline. The lithophysae are wrapped by the banding and therefore were in existence as solid objects while the volcanic material was still moving.

Chemical analyses of five samples of coherent rhyolite are given in Table 1. The rhyolite samples are chemically altered and are characterized by high values of K_2O, low Na_2O, and slightly elevated silica. Gee et al. (1976) argued that the Rb–Sr isochron date of 1098 ± 42 Ma obtained from the rhyolite is the age of this alteration event.

Felsic volcaniclastic rocks

Vogt (1995) documented the occurrence of felsic volcaniclastic rocks (lapilli tuff) near Cadabra Hill (MGA 671319E 7275608N). Here the volcaniclastic unit is 2 to 3 m thick and, although isolated, the underlying and overlying coarse-grained sandstone of the Kiangi Creek Formation is concordant within this succession. Lower levels of the volcaniclastic unit contain abundant, packed accretionary lapilli (Fig. 6b), up to 10 mm across. Some normal graded layers are present and the lapilli-rich layers are separated by thin lapilli-free layers (Vogt, 1995). In contrast, upper levels of the felsic unit comprise parallel planar-laminated to massive fine-grained volcanic sandstone.

In thin section the accretionary lapilli typically have coarse vesicular pumice shards in the core and fine-grained tangentially aligned platy shards forming the rim. Minor angular, sometimes embayed, quartz grains are present in the coarse-grained parts of the lapilli (Vogt, 1995).

Chemical analyses of three samples of felsic volcaniclastic rock are given in Table 1. As noted by Vogt (1995), the K-alteration shown by the coherent rhyolite did not affect the volcaniclastic rocks, which are impoverished in both K and Na, but enriched in Si. The volcaniclastic rocks also contain elevated levels of Ba and F. Field analyses with portable XRF equipment indicate Zr levels are significantly higher in the laminated to massive upper part of the volcaniclastic unit as compared with the lower, accretionary lapilli-bearing division.

Evidence for syndepositional emplacement

Beds of closely packed, locally graded, accretionary lapilli are interpreted as primary pyroclastic fall deposits, either from subaerial hydroclastic eruptions, or from eruptions where the moisture was supplied by rain falling through the eruption cloud (cf. Fisher and Schmincke, 1984). Upper levels of the volcaniclastic unit that display parallel lamination are regarded as reworked pyroclastic deposits. Gee et al. (1976) noted that pebbles of rhyolite occur in conglomerate immediately overlying one of the small rhyolite plugs located north of the Tangadee Homestead road. Rhyolite pebbles are also present in conglomerate overlying the laminated felsic volcanic sandstone and siltstone south of the Tangadee road (around MGA 683282E 7272144N). Collins and McDonald (1994) recorded the presence of rhyolite pebbles in conglomerate at the top of the Gap Well Formation around Abra. Although no location is given, the stratigraphic position, lithological description, and thickness indicates that this conglomerate also belongs to the lower part of the Kiangi Creek Formation (unit WC1 of Vogt, 1995).

Therefore, although it could be argued that the banded coherent rhyolite was emplaced as a younger, high-level intrusion, the nature of the volcaniclastic rocks and presence of rhyolite pebbles in the overlying sedimentary succession indicates that the rhyolite was emplaced and

Table 1. Chemical analyses of the Tangadee Rhyolite

Rock type	*Rhyolite*	*Rhyolite*	*Rhyolite*	*Rhyolite*	*Lapilli tuff*	*Lapilli tuff*	*Felsic pipe*	*Felsic volcani-clastic*	*Rhyolite*	
Source	*1*	*2*	*3*	*4*[a]	*5*[a]	*6*[b]	*7*[b]	*8*[c]	*9*[c]	
					Percentage					
SiO_2	78	76.1	74.9	83.4	79.7	85.23	76.45	87.30	77.09	
Al_2O_3	11.1	12.3	12.3	10.24	9.97	9.02	10.62	6.42	11.73	
Fe_2O_3	0.66	0.62	1.06	0.43	2.93	1.97	5.18	0.56	0.10	
MgO	0.02	0.02	0.23	0.17	0.71	1.03	1.92	0.35	-0.01	
CaO	0.1	0.06	0.04	0.18	0.11	0.07	0.08	0.02	0.01	ICP-MS
Na_2O	0.15	0.15	0.2	0.55	0.27	0.1	0.23	-0.01	0.07	
K_2O	9.06	9.21	10.45	9.66	3.59	1.99	0.04	1.81	9.33	
MnO_2	<0.01	<0.01	<0.01	<0.01	0.02	0.01	0.03	0.01	0.01	
TiO_2	<0.01	<0.01	<0.01	0.04	0.11	0.13	0.34	0.25	0.055	
P_2O_5	<0.01	<0.01	<0.01	<0.01	0.03	0.03	0.04	0.03	0.01	
$H2O^+$	0.51	0.8	0.29	nd	nd	2.95	1.13	–	–	
SO_3	0.04	0.03	0.03	nd	nd	0.03	0.03	0.06	0.01	
CR_2O_3	0.32	0.26	0.04	–	–	–	–	–	–	
LOI (grav)	nd	nd	nd	nd	nd	nd	nd	3.01	1.60	
					Parts per million					
Ag	nd	nd	nd	nd	nd	nd	nd	-0.6	-0.6	ICP-MS
Ars	nd	nd	nd	<0.2	<0.2	nd	nd	2.9	4.3	
Ba	nd	nd	nd	460	2 950	3 356	85	1 547	299	
Be	nd	nd	nd	<0.5	3	nd	nd	1.9	-0.3	ICP-MS
Bi	nd	nd	nd	<2	<2	nd	nd	0.77	0.14	ICP-MS
Cd	nd	nd	nd	<0.5	<0.5	nd	nd	-0.02	0.04	ICP-MS
Ce	nd	nd	nd	nd	nd	nd	nd	82.16	25.22	ICP-MS
Co	nd	nd	nd	<1	2	<1	3	nd	nd	
Cr*	2 189	1 779	274	325	85	26	16	41	3	
Cs	nd	nd	nd	nd	nd	nd	nd	2.8	1.04	ICP-MS
Cu	45	190	110	5	10	17	24	4	-1	
Dy	nd	nd	nd	nd	nd	nd	nd	3.72	5.36	ICP-MS
Er	nd	nd	nd	nd	nd	nd	nd	2.07	3.68	ICP-MS
Eu	nd	nd	nd	nd	nd	nd	nd	0.465	0.258	ICP-MS
F	nd	nd	nd	nd	nd	nd	nd	729	-50	ICP-MS
Ga	nd	nd	nd	nd	nd	nd	nd	9.3	10.2	ICP-MS
Gd	nd	nd	nd	nd	nd	nd	nd	4.62	4.75	ICP-MS
Ge	nd	nd	nd	nd	nd	nd	nd	4.1	1.5	ICP-MS
Hf	nd	nd	nd	nd	nd	nd	nd	3.27	3.72	ICP-MS
Ho	nd	nd	nd	nd	nd	nd	nd	0.75	1.15	ICP-MS
La	nd	nd	nd	nd	nd	nd	nd	43.12	9.8	ICP-MS
Lu	nd	nd	nd	nd	nd	nd	nd	0.32	0.66	ICP-MS
Mo	<10	<10	<10	2	1	nd	nd	0.4	-0.3	ICP-MS
Nb	nd	nd	nd	nd	nd	nd	nd	13.6	31.7	ICP-MS
Nd	nd	nd	nd	nd	nd	nd	nd	30.26	14.51	ICP-MS
Ni	nd	nd	nd	4	5	3	16	7	3	
Pb	110	110	65	6	46	nd	nd	99	3	
Pr	nd	nd	nd	nd	nd	nd	nd	8.18	3.26	ICP-MS
Rb	150	160	180	nd	nd	III	<1	81.2	139.4	
Sb	nd	nd	nd	nd	nd	nd	nd	0.9	-0.8	ICP-MS
Sc	nd	nd	nd	nd	nd	nd	nd	6	2	
Sm	nd	nd	nd	nd	nd	nd	nd	5.57	4.85	ICP-MS
Sn	nd	nd	nd	nd	nd	nd	nd	1.9	2.9	ICP-MS
Sr	20	20	20	18	71	57	83	30.2	9.4	
Ta	nd	nd	nd	nd	nd	nd	nd	0.51	4.3	ICP-MS
Tb	nd	nd	nd	nd	nd	nd	nd	0.64	0.81	ICP-MS
Th	nd	nd	nd	nd	nd	nd	nd	11.15	15.5	ICP-MS
U	nd	nd	nd	nd	nd	nd	nd	2.33	1.45	ICP-MS
V	<56	<56	<56	<1	14	28	12	25	2	
W	5	<5	<5	<10	<10	nd	nd	–	–	
Y	nd	nd	nd	nd	nd	nd	nd	25	35	
Yb	nd	nd	nd	nd	nd	nd	nd	2.22	4.5	ICP-MS
Zn	17	16	15	7	46	<1	24	4	-1	
Zr	nd	nd	nd	nd	nd	nd	nd	130	80	
Total (%)	**99.96**	**99.55**	**99.54**	**104.78**	**97.44**	**102.53**	**96.12**	**99.81**	**100.05**	

NOTES:

1, 2, 3 Tangadee Rhyolite, Coobarra Dome area (Gee et aI., 1976)

4, 7 Tangadee Rhyolite (Vogt, 1995)

5, 6 Lapilli tuff, south of Cadabra Hill, (Vogt, 1995)

8. Felsic volcaniclastic rock, south of Cadabra Hill, GSWA sample 149019

9. Flow-banded rhyolite, GSWA sample 149020

[a] Analyst: Chemex Labs Ltd, Canada. using ICP and AAS

[b] Analyst: Geology and Palaeontology Institute. University of Hamburg, West Germany, using XRF

[c] Analyst: Geoscience Australia, using XRF and ICP-MS (where indicated)

* Cr values in excess of 60 ppm for samples 1–6 are probably analytical artefacts

partially eroded at the time of Kiangi Creek Formation sedimentation.

Discovery, Devil Creek, and Ullawarra Formations

The Kiangi Creek Formation has a sharp contact with the overlying chert and silicified siltstone of the Discovery Formation. The Discovery Formation is in turn overlain by the Devil Creek Formation, which comprises deep marine-shelf planar-laminated and ripple cross-laminated dolostone, dolomitic siltstone, and sandstone. The overlying Ullawarra Formation is the uppermost exposed unit of the Edmund Group and is largely composed of deep marine siltstone but with minor fine-grained sandstone, dolostone, and chert. A single occurrence of felsic volcaniclastic rock has been found in the upper part of this unit on Calyie (MGA 667860E 7263760N). It comprises highly silicified, fine- to very coarse-grained volcanic sandstone and breccia, with angular to rounded lapilli.

Collier Basin

The Collier Group has an estimated thickness of about 2 to 2.5 km and is separated from the underlying Edmund Group by a low-angle disconformity (Martin et al., 2005). It is subdivided, in ascending order, into the Backdoor, Calyie, and Ilgarari Formations. The minimum age of the Collier Group is constrained by c. 1070 Ma sills of Kulkatharra Dolerite that were intruded into both the Collier Group and the underlying Edmund Group (Wingate, 2002). These sills were intruded into wet sediments (Martin, 2004), indicating that the depositional age of the Collier Group is close to 1070 Ma and significantly younger than the Edmund Group.

The Backdoor Formation is the lowest unit of the Collier Group exposed around Abra. It comprises deep marine mudstone, and subordinate thin- to thick-bedded sandstone, together with minor chert and dolostone. These rocks are overlain by submarine fan deposits of the Calyie Formation, comprising thick-bedded fine- to medium-grained quartz sandstone and siltstone. The overlying Ilgarari Formation is also dominated by deeper marine deposits, consisting of siltstone, mudstone, and fine-grained sandstone.

Paleoproterozoic to Neoproterozoic tectonothermal history of the Capricorn Orogen

The results of recent mapping and geochronology studies from the Capricorn Orogen have been discussed by Occhipinti et al. (2001), Cawood and Tyler (2004), Sheppard (2004), Martin et al. (2005), Sheppard et al. (2006, 2007), and Johnson et al. (2009). These studies have shown that the Capricorn Orogen underwent numerous tectonothermal events during the Paleoproterozoic to Neoproterozoic. During the Paleoproterozoic the most important events were the c. 2200 Ma Ophthalmian Orogeny, the 2005–1950 Ma Glenburgh Orogeny, the 1830–1780 Ma Capricorn Orogeny, and the 1680–1620 Ma Mangaroon Orogeny (Cawood and Tyler, 2004; Occhipinti et al., 2001; Sheppard et al., 2005).

1620–1465 Ma Edmund Basin and Narimbunna Dolerite

Several major tectonothermal events also affected the Capricorn Orogen during the Mesoproterozoic and Neoproterozoic. The Edmund Basin was initiated after 1620 Ma during intracratonic extensional reactivation of older Capricorn Orogen structures (Martin et al., 2005). Apart from the Tangadee Rhyolite, proven occurrences of felsic igneous activity within Edmund Group are rare. A localized felsic volcaniclastic unit lies within the Ullawarra Formation (upper Edmund Group) on Milgun and yielded a SHRIMP U–Pb zircon age of 1460 ± 9 Ma (Wingate et al., in prep.). This age is within error of c. 1465 Ma ages reported for the Narimbunna Dolerite that intrudes the Edmund Group over much of the Edmund Basin (Wingate, 2002; Morris and Pirajno, 2005).

Collier Basin and 1280–1250 Ma event

Deposition of the Edmund Group was followed by an interval of up to 390 million years during which the Edmund Group was tilted gently towards the west and southwest, and eroded, before regional subsidence initiated the Collier Basin. Johnson et al. (2009) recorded that garnet–staurolite schists of the Leake Spring Metamorphics (formerly Morrissey Metamorphics) in the Gascoyne Province on Eudamullah contain a well-developed medium-grade crenulation schistosity. Monazites parallel to relict, folded S_1 fabrics within garnet and staurolite porphyroblasts give consistent ages of c. 1280 Ma, whereas those within the main S_2 fabric give ages of c. 1250 Ma (Johnson et al., 2009). Currently the extent and significance of this c. 1280–1250 Ma event is unknown.

1078–1070 Ma Warakurna Large Igneous Province

Voluminous sills of the Kulkatharra Dolerite were intruded into the Collier and Edmund Groups at c. 1070 Ma (Wingate, 2002). These sills can be correlated with mafic intrusions of a similar age that have been identified well beyond the limits of the Edmund and Collier Basins, and constitute the 1078–1070 Ma Warakurna Large Igneous Province (Wingate et al., 2004; Morris and Pirajno, 2005). The 1098 ± 42 Ma alteration event recorded by Gee et al. (1976) in the Tangadee Rhyolite may also be related to the Warakurna Large Igneous Province.

1030–950 Ma Edmundian Orogeny

Rocks in the Edmund and Collier Basins and the underlying basement were deformed and subjected to low- to high-grade metamorphism during the 1030–950 Ma Edmundian Orogeny (Martin et al., 2005; Sheppard et al., 2007; Johnson et al., 2009). Over much of the Edmund Fold Belt the orogeny largely resulted in north–south shortening and sinistral transpression and formed easterly to southeasterly trending, open to tight, upright folds and normal, reverse, and strike-slip faults. On Mount Phillips the Ti Tree Shear Zone forms a major sinistrally transpressive discontinuity that separates medium-grade mid-amphibolite facies crust in the southwest (Mutherbukin zone) from low-grade upper crust to the northeast (Sheppard et al., 2007; Johnson et al., 2009). Metamorphic zircon extracted from sinistral melt pockets within a c. 1665 Ma metamonzogranite in the Mutherbukin zone, gave a precise SHRIMP U–Pb crystallization age of 1000 ± 8 Ma (Wingate et al., 2010), dating the main phase of sinistral-transpressional movement on the Ti Tree Shear Zone (Johnson et al., 2009).

900–820 Ma event

Edmundian Orogeny fabrics within the northern Mutherbukin zone of the Gascoyne Province are cut by the undeformed 'Gurun Gutta granite' (Sheppard et al., 2007; Johnson et al., 2009). Preliminary SHRIMP U–Th–Pb geochronology of monazite from this granite yielded a date of c. 910 Ma, interpreted as the age of igneous crystallization (Johnson et al., 2009). Occhipinti, (2007) obtained $^{40}Ar/^{39}Ar$ mica dates of 960 to 820 Ma from various rock units from the Errabiddy Shear Zone and southern Gascoyne Complex.

c. 570 Ma Mulka Tectonic Event

Gascoyne Province and Bangemall Supergroup rocks are cut by late-stage brittle–ductile faults and shears and associated quartz veins. These commonly have well-developed dextral strike-slip shear-sense indicators, and they show dextral offset of dolerite dykes belonging to the c. 755 Ma Mundine Well dyke swarm. Shearing and faulting are dated at c. 570 Ma by in situ $^{40}Ar/^{39}Ar$ on newly grown muscovite in a small dextral shear zone (Martin et al., 2007).

Mineralization

The Abra mineralization was described by Vogt and Stumpfl (1987), Boddington (1990), Collins and McDonald (1994), and Vogt (1995), and reported on in Cooper et al. (1998). Austen (2007) carried out a petrographic, fluid inclusion, and isotopic study of the Abra deposit. Pirajno et al. (2009) carried out a more-recent study and the following account is based on this work.

This polymetallic deposit is hosted by siltstone, dolostone, and sandstone rocks of the Irregully and Kiangi Creek Formations, but the zone of widespread mineralization does not extend above an erosion surface marking the change from fluvial to marine and fan-delta facies in the lower part of the Kiangi Creek Formation (Thorne et al., 2009). Isolated veins of barite, chalcopyrite, dolomite, and galena up to 10 mm wide are, however, recorded in the marine and fan-delta facies overlying the major mineralization.

The Abra deposit comprises a funnel-shaped brecciated zone, interpreted as a breccia feeder-pipe, overlain by stratabound mineralization. The stratabound mineralization includes a Red Zone and an underlying Black Zone. The Red Zone is dominated by barite, banded jaspilite, hematite, galena, pyrite, quartz, abundant barite, and siderite. The Black Zone comprises veins and rhythmically banded galena, sphalerite, and pyrite, with minor tetrahedrite, chalcopyrite, and scheelite. These ore minerals are associated with laminated and/or brecciated hematite, magnetite, Fe-rich carbonate, barite, and scheelite. In both the Red and Black Zones laminations and bands of ore minerals, iron oxides, barite, and quartz commonly exhibit colloform textures. The breccia feeder-pipe (called the stringer zone) merges with the Black Zone and consists of a stockwork of iron carbonate and quartz, barite, pyrite, magnetite, and chalcopyrite veins and disseminations, with abundant fluidized and/or jigsaw textures that cut through a wider alteration envelope of chlorite and siderite in rock units of the Irregully Formation (Pirajno et al., 2009). Boddington (1990) noted that the upper part of the stringer zone contains higher Ba–Ag–Pb than the lower parts, which are enriched in Cu–Au.

The Abra mineral system records multiple overprinting phases of hydrothermal activity that have resulted in several stages of brecciation and fluidization, barite, and sulfide veining, and barren low-temperature chalcedonic (epithermal style) veining (Pirajno et al., 2009). Hydrothermal alteration minerals include multi-stage quartz, chlorite, prehnite, Fe-rich carbonate, and albite. Albite (Na-metasomatism) is an early alteration phase, whereas Fe-rich carbonate is a late phase. Fluid inclusion studies by Austen (2007) suggested that the metals may have been derived from the sedimentary rocks and that the ore fluids had temperatures ranging from 162 to 250°C, with salinities ranging from 5.8 to about 20 wt% NaCl. The sulfur isotopic system shows $\delta^{34}S$ values ranging from 19.4 to 26.6‰ for sulfides (chalcopyrite, pyrite, sphalerite, galena) and from 37.4 to 41.9‰ for barite (Vogt and Stumpfl, 1987; Austen, 2007). Sulfur isotope thermometry between sulfides and sulfide–barite pairs yield values ranging from 219 to 336°C, whereas oxygen isotope thermometry from coexisting pairs (e.g. quartz–chlorite and hematite–magnetite) show a wider range of temperatures, from 228 to 452°C (Austen, 2007).

Vogt and Stumpfl (1987) and Collins and McDonald (1994) linked the genesis of the Abra deposit to c. 1.64 Ga rift-related tectonics and felsic magmatism, and suggested that the source of the lead and barium may have been the associated arkosic sediments. The association of the deposit with felsic magmatism in a rift setting, together with Fe-rich and chlorite alteration of the host sedimentary rocks, raises the possibility that the Abra deposit may be

a variant of the Iberian Pyrite Belt (IPB) mineral systems, which are typically associated with thick siliciclastic successions in a rift setting and exhibit widespread chloritic alteration. Recent work on IPB systems by Tornos (2006) and Tornos and Heinrich (2007), supported the idea of a genetic relationship between the sulfide mineralization and siliciclastic sedimentary successions as the metal source. Tornos and Heinrich (2007) also envisaged that heat may be provided by an underlying igneous source and a mechanism of sulfide precipitation by mixing of S-deficient metalliferous brines with biogenic H_2S-rich fluids. They pointed out that the IPB (and Abra) mineral systems share features that are common with sedimentary exhalative (SEDEX) systems, rather than with volcanogenic associations. However, the IPB deposits have an undeniable link with coeval felsic magmatism and this would support a volcanogenic association. The case is less clear for Abra, although there appears to be a *spatial* link with felsic volcanism, represented by the Tangadee Rhyolite, which is stratigraphically part of the Kiangi Creek Formation and outcrops in the vicinity of the deposit.

Pirajno et al. (2009) proposed a genetic model in which basinal fluids were possibly heated by the magmatic system associated with the Tangadee Rhyolite. Alternatively, the voluminous mafic sills that intrude the sedimentary rocks of the Edmund Basin may have provided the thermal energy. Heating of basinal fluids and of pore fluids could have caused rapid expansion and boiling, resulting in eruption or venting of hydrothermal fluids and the inception of pipe-like structures (stringer zone). These eruptions would have re-occurred, resulting in several stages of hydrothermal activity, with multiphase hydrofracturing and overprinting textures (Black Zone) at several localities. The hydrothermal eruptions also deposited chemical sediments, represented by laminated iron oxides and barite (Red Zone). The abundance of barite can be explained by leaching of evaporitic minerals in the sedimentary succession. The model suggests that there may be several of these hydrothermal breccia pipes and that each of these pipes would be associated with distal hematite–barite chemical sediments, enhancing the prospectivity of the Jillawarra Basin.

Samples

This study is based on 12 sandstone samples (GSWA sample nos 149084–95) obtained from Abra diamond drillhole core (drillholes AB58, AB36, and AB22b) and one sample from an outcrop of the coherent facies of the Tangadee Rhyolite (GSWA sample no. 149020). The locations and stratigraphic positions of the samples are given in Table 2 and Figure 7. The Abra core material was collected from non-mineralized parts of the Kiangi Creek (West Creek) Formation that overlie the mineralization (GSWA sample nos. 149089–90), as well as mineralized sandstones from within the ore body. The latter comprise sandstones from near the base of the Kiangi Creek Formation (GSWA 149084–88) and from the underlying Irregully (Gap Well) Formation (GSWA 149091–95).

Table 2. Locations of samples used in this study

GSWA sample no.	*Abra sample no.*	*Drillhole ID*	*Depth from (m)*	*Depth to (m)*	*Lithology*	*Stratigraphic unit*	*MGA Zone 50 Easting*	*Northing*
149084	AB011270	AB58	371.8	372	conglomerate	Lower Kiangi Creek fluvial facies (WC1; Vogt (1995))	660275	7273633
149085	AB011271	AB58	373.4	373.6	conglomerate	Lower Kiangi Creek fluvial facies (WC1; Vogt (1995))	660275	7273633
149086	AB011272	AB58	370.3	370.6	conglomerate	Lower Kiangi Creek fluvial facies (WC1; Vogt (1995))	660275	7273633
149087	AB011273	AB58	360.8	360.97	sandstone	Lower Kiangi Creek fluvial facies (WC1; Vogt (1995))	660275	7273633
149088	AB011274	AB58	358.55	358.79	sandstone	Lower Kiangi Creek fluvial facies (WC1; Vogt (1995))	660275	7273633
149089	AB011275	AB58	120.48	120.7	sandstone	Middle Kiangi Creek marine facies (WC2; Vogt (1995))	660275	7273633
149090	AB011276	AB58	111.5	111.85	sandstone	Middle Kiangi Creek marine facies (WC2; Vogt (1995))	660275	7273633
149091	AB011277	AB58	510.55	510.96	sandstone	Irregully Formation (Gap Well; Vogt (1995))	660275	7273633
149092	AB011278	AB58	497.2	497.5	sandstone	Irregully Formation (Gap Well; Vogt (1995))	660275	7273633
149093	AB011279	AB50	784.57	784.84	sandstone	Irregully Formation (Gap Well; Vogt (1995))	660575	7273712
149094	AB011280	AB36	779.82	780.03	sandstone	Irregully Formation (Gap Well; Vogt (1995))	660122	7273154
149095	AB011281	AB22B	775.28	775.6	sandstone	Irregully Formation (Gap Well; Vogt (1995))	660602	7273723
149020	–	Outcrop	–	–	rhyolite	Tangadee Rhyolite	680817	7276345

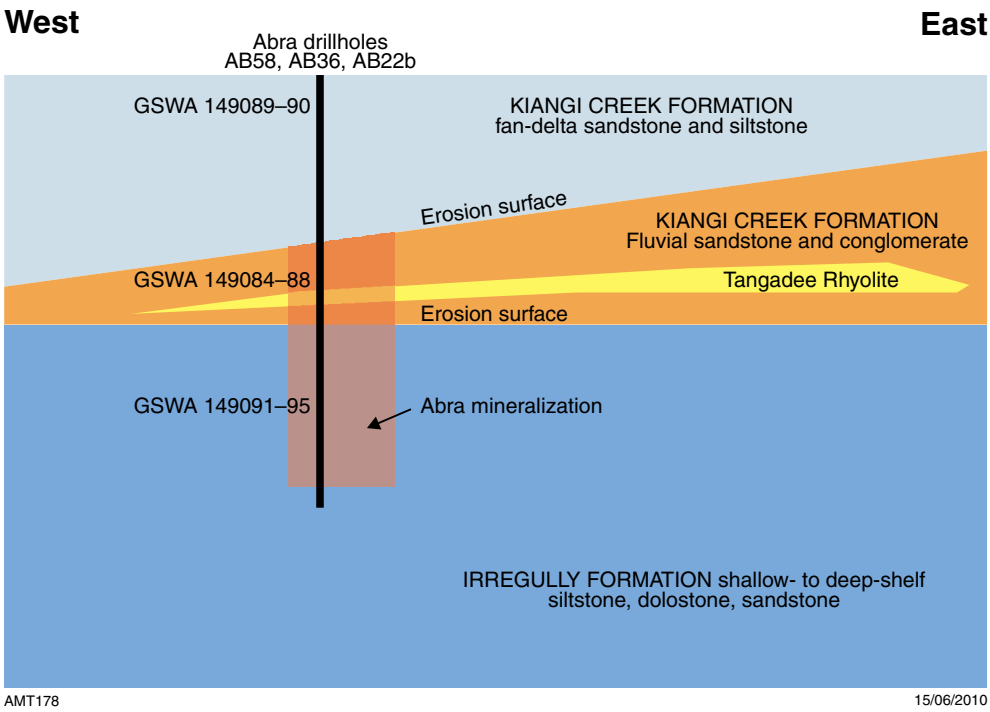

Figure 7. Schematic representation of Abra host-rock stratigraphy and sample locations. Vertical thickness not to scale. The presence of Tangadee Rhyolite in the mineralized succession at Abra has not been confirmed.

Analytical methods

SHRIMP analyses of monazite, xenotime, and zircon grains in the twelve sandstone samples were all made in situ. Polished thin sections prepared from the sandstone samples were examined using back-scattered electron microscopy (BSEM) to identify suitable grains. Portions of the thin sections containing grains large enough for in situ geochronology (>10 µm) were drilled out in ~3 mm discs, which were cast in 25 mm epoxy mounts.

Xenotime and zircon extracted from flow-banded Tangadee Rhyolite sample 149020 were analysed in GSWA grain mount G08-3. Procedures for zircon separation and mount manufacture follow those detailed in Wingate and Kirkland (2009). High-contrast BSEM imaging identified xenotime outgrowths on one zircon grain, and zoned cores in some of the discrete xenotime grains. The U–Pb and Th–Pb analyses, including those of zircon, utilized the high spatial-resolution capability of SHRIMP, with 0.2–0.3 nA O_2^- primary ion beams focused onto ~10 µm spots. Established SHRIMP operating procedures and data-reduction schemes were used for zircon (e.g. Williams, 1998) and xenotime analyses (Fletcher et al., 2000; 2004). Data acquisition for monazite also followed established practice (Foster et al., 2000) although new data-reduction procedures and corrections for matrix effects were applied (Fletcher et al., 2010). Squid-2 software (Ludwig, 2009) was used for initial data reduction. Corrections for matrix effects in $^{206}Pb/^{238}U$ and $^{208}Pb/^{232}Th$, and for instrumental mass fractionation in $^{207}Pb/^{206}Pb$, were applied to data from xenotime (Fletcher et al., 2004) and monazite (Fletcher et al., 2010) in spreadsheet templates.

Results

Petrography

Abra deposit

Samples from the Edmund Group are sandstones comprising medium- to coarse-grained quartz with subordinate K-feldspar. Detrital muscovite is rare and was only observed in a sample devoid of chlorite alteration. Lithic fragments are common, and include rounded to elongate sericitic grains (after ?shale), chert, fine- to coarse-grained sandstone and siltstone, metasedimentary rocks, and fine-grained silica with mylonitic seams. Quartz grains are predominantly subrounded to rounded and are engulfed by syntaxial quartz overgrowths (Fig. 8a,b). The quartz overgrowths are commonly riddled with fluid inclusions. In some samples, a dark film is evident around detrital quartz grains (Fig. 8a,b). Also, some quartz grains (and overgrowths) are cut by intragranular and transgranular fractures, marked by dense trails of fluid inclusions (Fig. 8c,d). Some pockets of matrix, comprising mostly chlorite and siderite, also contain euhedral and prismatic quartz of possible hydrothermal origin (Fig. 8e,f).

K-feldspar is relatively common in most samples as detrital grains. Several samples (e.g. 149084; 149086) contain K-feldspar with significant overgrowths of Ba-rich feldspar (Fig. 9a,b). The Ba-rich K-feldspar is best developed where detrital grains are adjacent to matrix (Fig. 9a,b). Scanning electron microscope–cathodoluminescence (SEM-CL) imaging was used to distinguish detrital

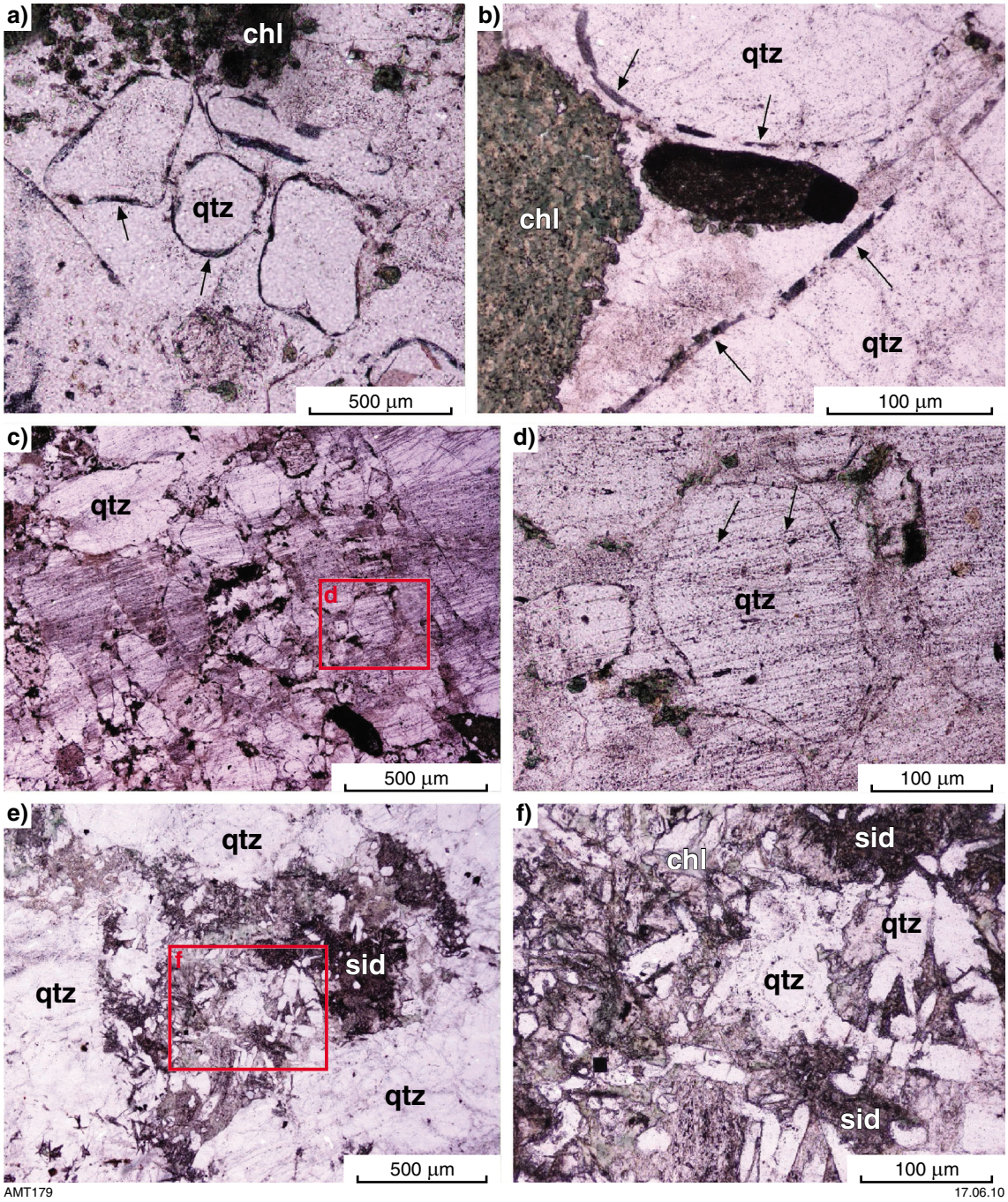

Figure 8. a) and b) Plane polarized light (PPL) images of detrital quartz grains (qtz) with a dark film lining the boundary between detrital and authigenic quartz (see arrows). In b), an elongate clast has been largely replaced by siderite and is engulfed in authigenic quartz; c) and d) PPL images of quartz transected by a dense array of fluid inclusion trails that cut both detrital and authigenic quartz, indicating that the fine fractures formed after lithification; e) and f) PPL images of a large pocket of matrix between detrital quartz grains filled with siderite (sid), chlorite (chl), and hydrothermal quartz. a) and b) — sample 149084; c) and d) — sample 149085; e) and f) — sample 149094.

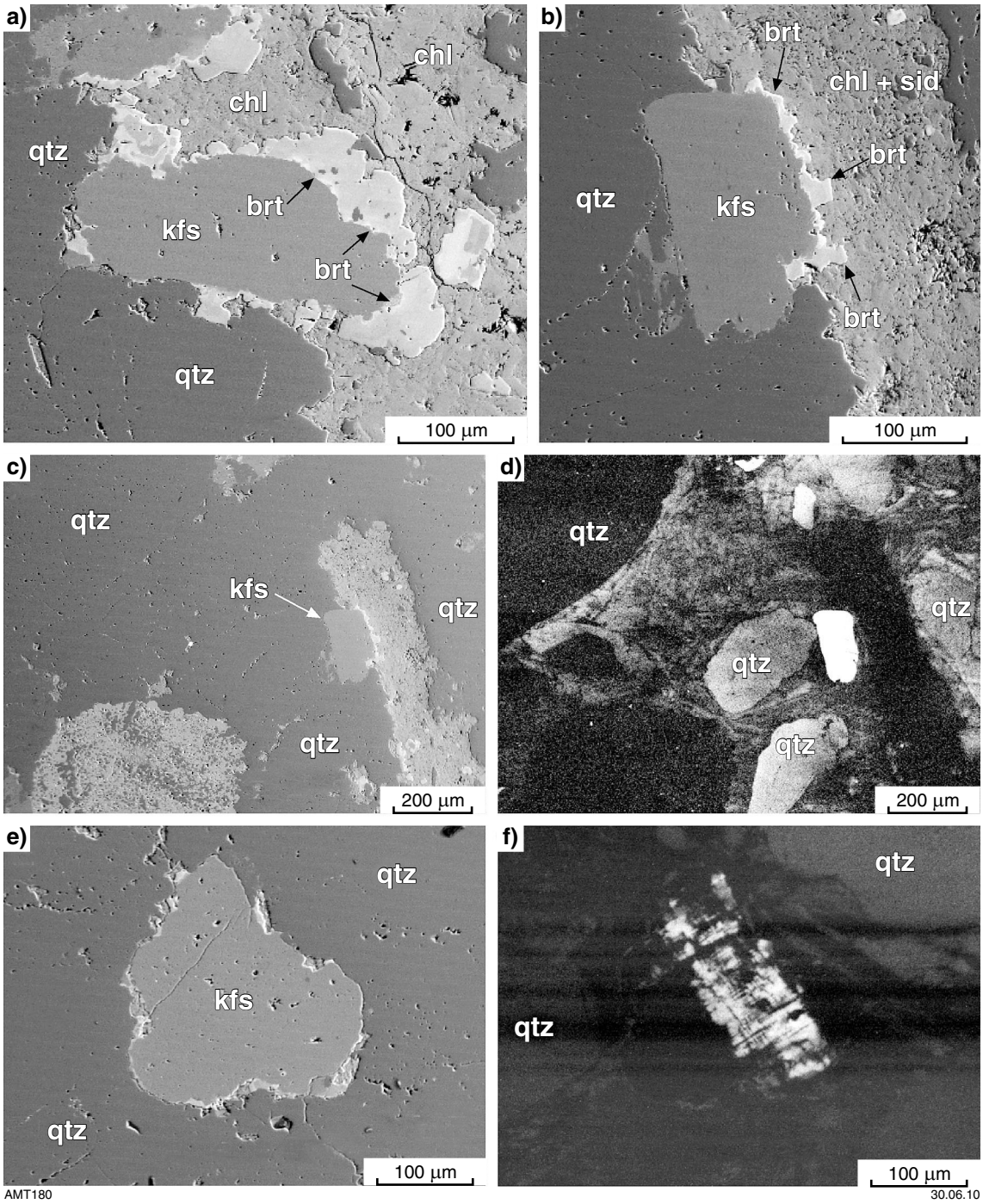

Figure 9. **Back-scattered electron (BSE) images of K-feldspar in the sandstone (sample 149084) hosting the Abra mineralization: a) and b) BSE images showing elongate K-feldspar (kfs) grains with thick rims of Ba-rich (brt) K-feldspar developed in the portion facing the matrix, which comprises mostly chlorite (chl) and siderite (sid); c) BSE image of portion of sandstone showing quartz (qtz), K-feldspar (kfs) and siderite (sid); d) SEM-cathodoluminescent (SEM-CL) image of 9c showing subrounded detrital quartz (qtz) and detrital K-feldspar (white). Note the presence of extensive, zoned authigenic quartz between the detrital quartz; e) BSE image of a K-feldspar grain; f) SEM-CL of same K-feldspar as in 9e showing a highly corroded detrital core (white) and substantial authigenic K-feldspar overgrowth (black; non-luminescent).**

quartz and K-feldspar from low-temperature authigenic overgrowths (Fig. 9c,d). SEM-CL imaging of K-feldspar grains reveal significant dissolution of detrital grains and, in some cases, substantial growth of authigenic feldspar (Fig. 9e,f).

The main matrix mineral is chlorite, which may occur with sericite. Carbonate minerals are present in most samples and comprise predominantly siderite. Dolomite was also identified in samples 149093 and 149087.

Sulfides are abundant in some samples and include pyrite, chalcopyrite, galena, sphalerite, a Cu–Sb–S mineral (sample 149084), and an Fe–Ni–Co–As–S mineral (149090), shown in Figure 10a. Several samples from the mineralized zone (149093; 149094) also contain a tungsten-rich mineral, with minor Fe and Mn (probably wolframite; Fig. 10b). A second W-rich mineral (probably scheelite) was identified in sample 149084, comprising mostly W and minor Ca.

Magnetite is present in several samples (149093; 149090) as detrital grains and as a post-depositional phase. Barite, apatite, rutile, tourmaline, and a Th-silicate mineral were also found in several samples. An inclusion of uraninite was identified in a single detrital quartz grain.

Zircon grains are present in most samples, and occur as rounded to euhedral grains in the sandstone matrix and as primary inclusions in detrital quartz grains (Fig. 10c,d). Xenotime was found in most samples, mainly as detrital grains or as inclusions within detrital quartz (Fig. 10e). Xenotime also occurs as rare overgrowths on detrital zircon grains (Fig. 10f). Monazite was found in most samples as euhedral inclusions within detrital quartz (Fig. 11a). Small irregular grains or aggregates of hydrothermal monazite (Fig. 11b–f) are present in the chlorite–carbonate matrix of several of the mineralized samples (e.g. 149094; 149093; 149086; 149085).

Tangadee Rhyolite

SHRIMP mount G08-3 (sample 149020) contains a small population of semi-opaque zircon crystals (Fig. 12a,b) amongst a larger population of equant, clear xenotime crystals. A single ?xenocrystic zircon grain contains a thick overgrowth that comprises xenotime intergrown with lozenge-shape K-feldspar grains (Fig. 12c,d). Most xenotime crystals are euhedral and equant, and up to 100 μm in size. Most crystal surfaces are planar, but locally, xenotime is intergrown with cassiterite (Fig. 12e,f), K-feldspar, kaolinite, and rutile. High-contrast back-scattered electron (BSE) imaging of the xenotime reveals the presence of two discrete zones. Most grains have a discrete core that displays strong oscillatory zoning and a typically larger, compositionally homogenous rim (Fig. 12g,h). In places, the oscillatory zoning is truncated (Fig. 12h), indicating possible dissolution and reprecipitation of the xenotime core.

SHRIMP geochronology

In the following sections, $^{207}Pb/^{206}Pb$ dates from single analyses are reported with 1σ internal precisions. Weighted mean $^{207}Pb/^{206}Pb$ dates are reported with 95% confidence limits.

Zircon

The zircon data in this study are ancillary to the monazite and xenotime data. There are only a few analyses of each sample, and the concurrent data for reference zircons in each analytical session are also limited. The reduced beam currents that were utilized further limit the data quality, so these data are not equivalent to those from datasets designed primarily for zircon geochronology. The data for the various samples are listed together in Table 3.

Kiangi Creek sandstone hosting Abra mineralization (GSWA 149084, 149087)

The sample grains were in ~3 mm discs plug-drilled from polished thin sections, cast in mount BR09-03. The reference zircon was CZ3 (Pb/U age 561.5 Ma), fragments of which were set in a separate 3 mm polished disc that was cast in the mount.

The SHRIMP was operated with a ~50 μm Kohler aperture in the primary ion column, giving a ~0.35 nA primary ion beam (O_2^-); and a ~15 × 10 μm analysis spot. The secondary ion mass resolution (M/ΔM at 1% of peak height) was ~5000. The post-collector retardation lens was not activated. Seven scans of the mass spectrum were recorded for each analysis. The 1σ external precision of $^{206}Pb/^{238}U$ was 2.64%.

Three analyses were made on two zircon grains (Table 3). Grain 0903B.1, an inclusion in detrital quartz, gave a $^{207}Pb/^{206}Pb$ date of 2000 ± 9 Ma. Combined data for two analyses of grain 0903E.1, a discrete grain in the matrix, gave 1948 ± 18 Ma (1σ). Both dates are consistent with a detrital origin of the grains.

Irregully Formation sandstone hosting Abra mineralization (GSWA 149093)

The sample grains were in ~3 mm discs plug-drilled from polished thin sections, cast in mount BR09-06. The reference zircon was grains of the Temora standard (Pb/U age 417 Ma) and fragments of CZ3, both in separate mounts that were cleaned and Au-coated with BR09-06.

A ~40 μm Kohler aperture was used, giving ~0.25 nA primary ion beam (O_2^-) and a ~15 x 10 μm analysis spot. The mass resolution was ~5050. Seven scans of the mass spectrum were recorded for each analysis. The analyses were carried out in conjunction with xenotime analyses and therefore the retardation lens was activated, although the correction for mass fractionation was insignificant. The 1σ external precision propagated to $^{206}Pb/^{238}U$ for the sample zircons was 3.8%.

Two analyses were obtained solely to enable corrections for zircon incorporated in the analysis of xenotime overgrowths on these grains. Grain 0906A.2 gave a $^{207}Pb/^{206}Pb$ date of 2457 ± 15 Ma but data from 0906E.2 are highly discordant and do not give a reliable date.

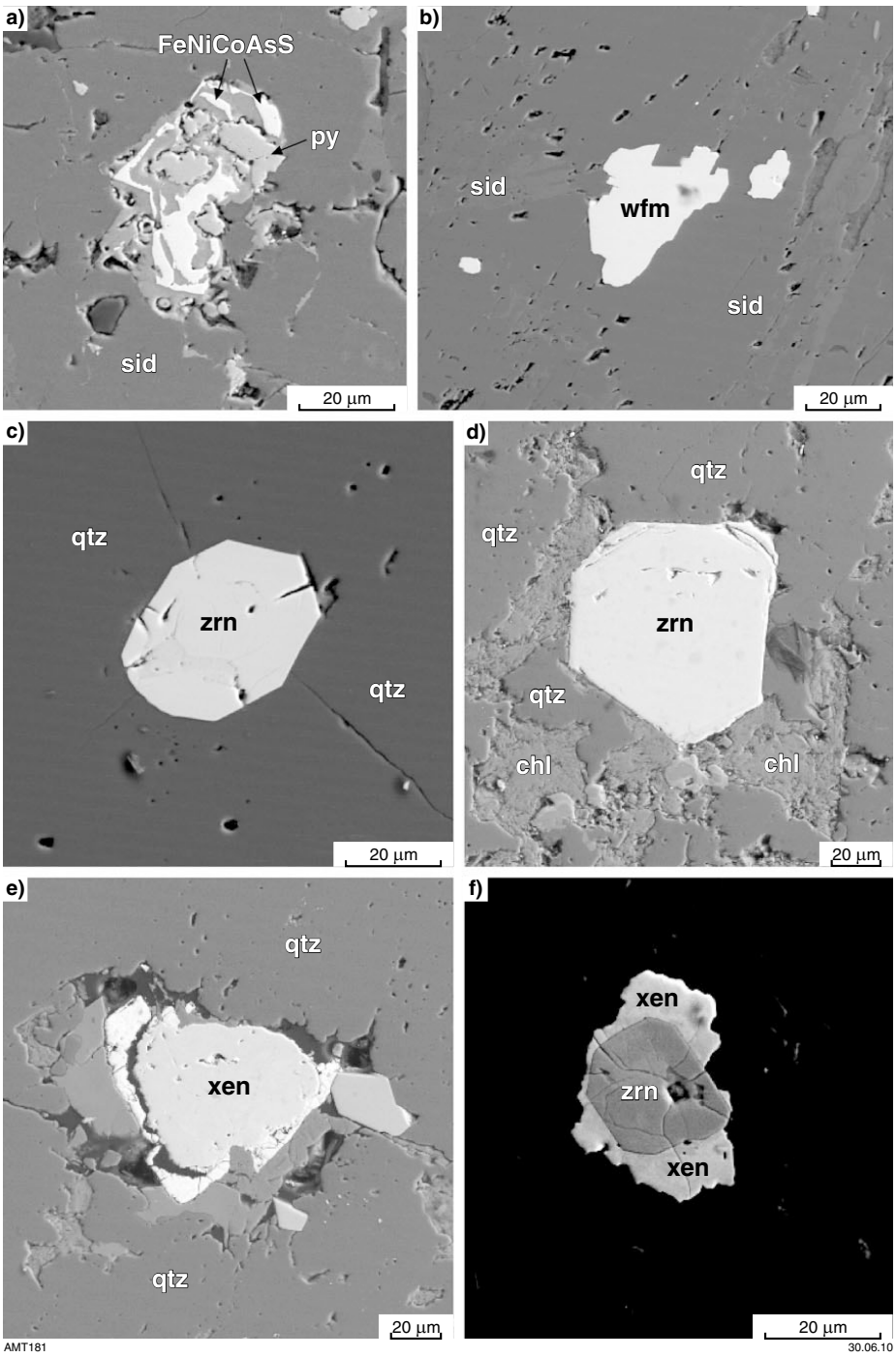

Figure 10. **Back-scattered electron (BSE) images: a) BSE image of a complex grain comprising pyrite and a Fe–Ni–Co–As–S mineral. The grain is engulfed by siderite; b) BSE image of wolframite (wfm) grains enclosed in siderite (sid); c) BSE image of a euhedral zircon (zrn) inclusion with radial cracks within a detrital quartz grain (qtz); d) BSE image of an euhedral zircon grain (zrn) in the matrix of a quartz sandstone. Surrounding minerals are chlorite (chl) and quartz (qtz); e) BSE image of a sub-rounded detrital xenotime grain (xen) surrounded by detrital quartz (qtz); f) High-contrast BSE image of zircon (zrn) surrounded by authigenic xenotime (xen). a) — 149090; b), c) — 149094; d) — 149084, SHRIMP grain 0903E; e) — 149085, SHRIMP grain 0906M; f) — 149093, SHRIMP grain 906C.**

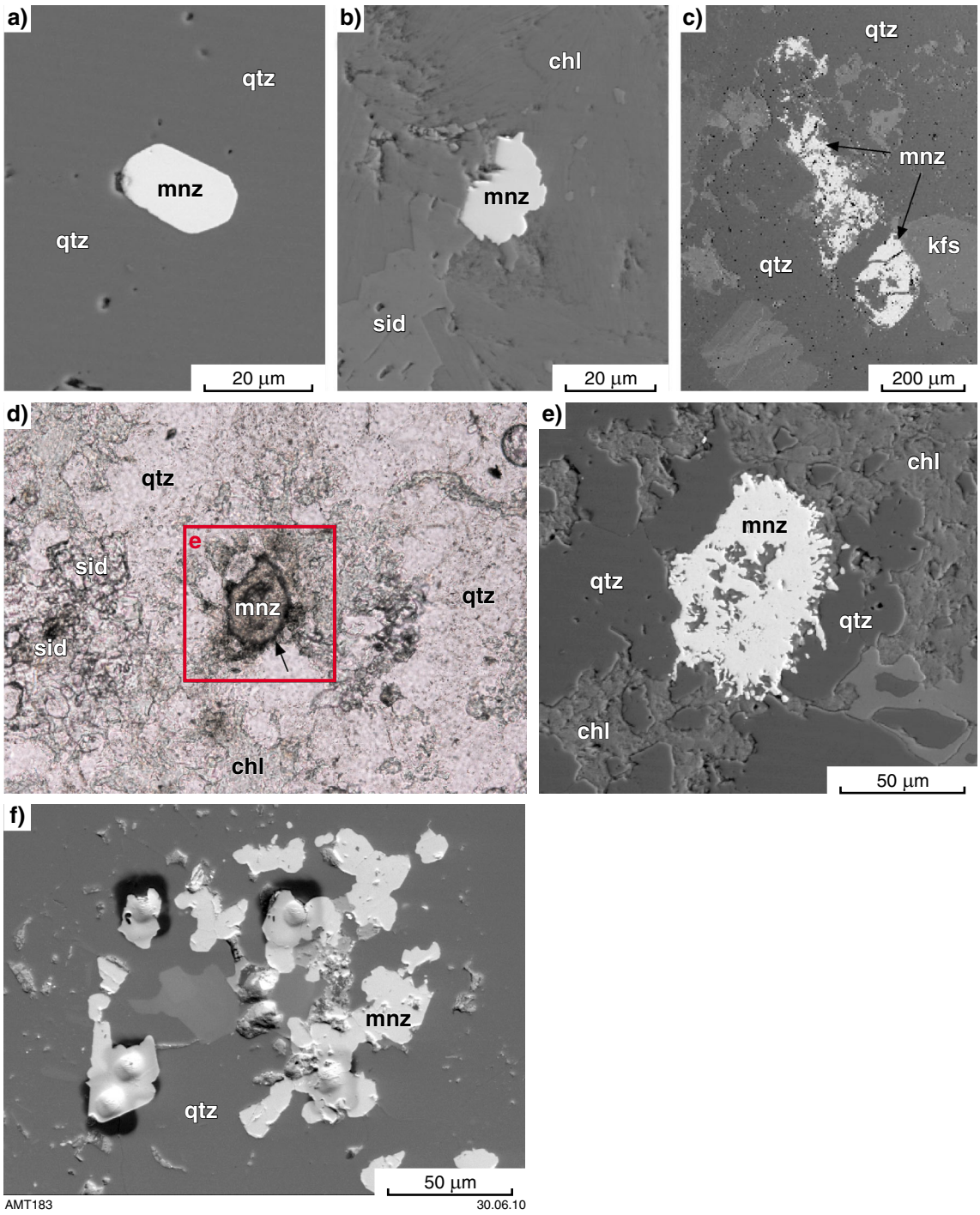

Figure 11. Back-scattered electron (BSE) images: a) BSE image of euhedral monazite (mnz) inclusion in detrital quartz (qtz); b) Irregular hydrothermal monazite (mnz) enclosed by chlorite (chl) and siderite (sid); c) BSE image of a large hydrothermal monazite (mnz) aggregate; d) PPL image of hydrothermal monazite (mnz) in sandstone matrix comprising chlorite (chl), siderite (sid) and authigenic quartz (qtz); e) BSE image of monazite in 11d showing the irregular shape of the monazite aggregate and the presence of abundant mineral inclusions. f) monazite aggregate showing five oval SHRIMP pits and surrounding raster burn areas. a) — 149089, SHRIMP grain 0905H; b) — 149094, SHRIMP grain 0904L; c) — 149085, SHRIMP grain 0904B; d), e) — 149093, SHRIMP grain 0904G; f) — 149086, SHRIMP grain 0904K.

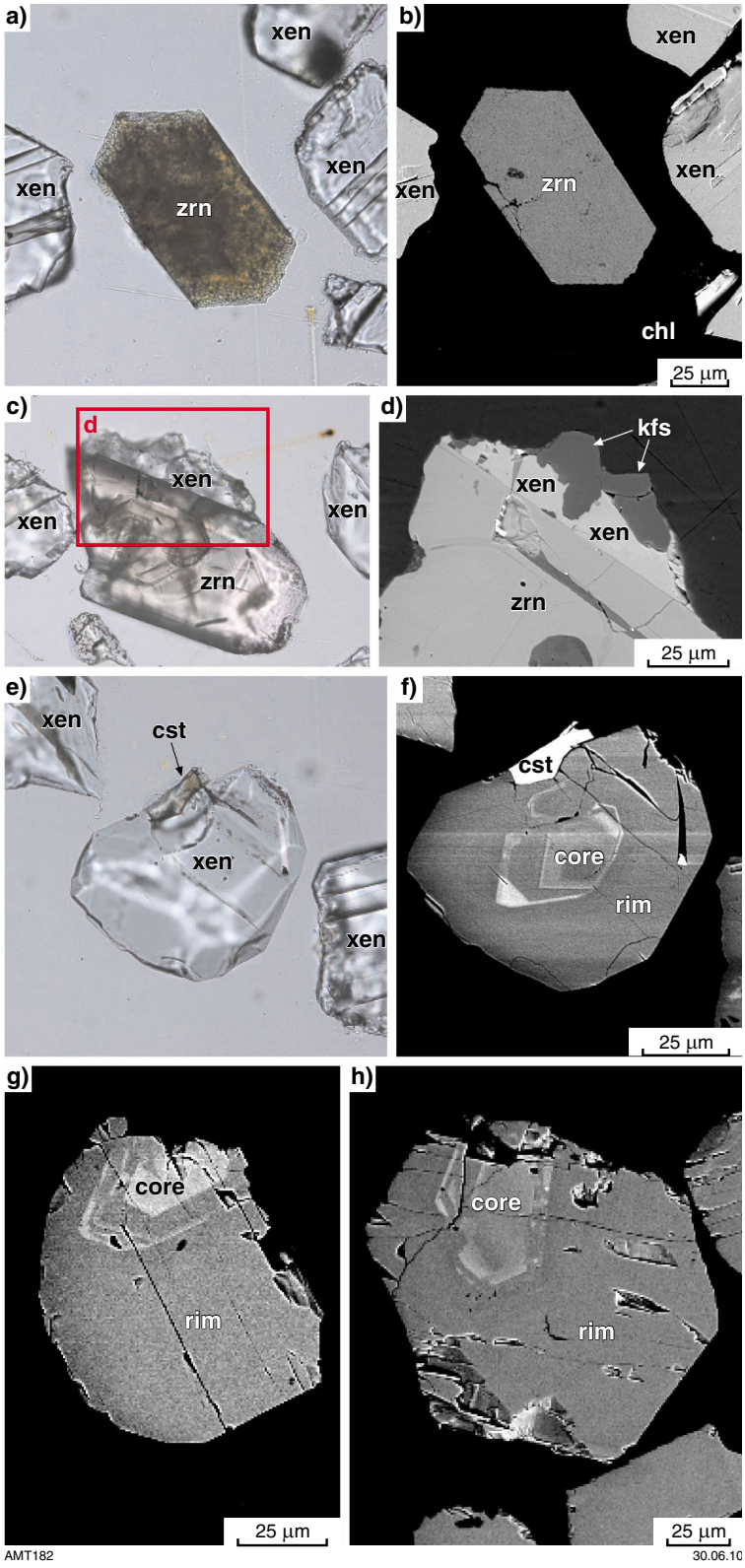

Figure 12. **Heavy mineral separates from GSWA mount G08-3 (sample 149020): a) PPL image of euhedral (magmatic?) zircon (zrn) from the Tangadee Rhyolite (SHRIMP grain G08-3L); b) BSE image of 12a showing an irregular mottled surface (SHRIMP grain G08-3L); c) PPL image of ?xenocrystic zircon (zrn) with a thick overgrowth (SHRIMP grain G08-3A); d) BSE image of 12c (SHRIMP grain G08-3A) showing authigenic xenotime (xen) on zircon (zrn) partly intergrown with K-feldspar (kfs); e) PPL image of a transparent xenotime (xen) with planar faces intergrown with cassiterite (cst) (SHRIMP grain G08-3D); f) BSE image of e) (SHRIMP grain G08-3D) showing the presence of a strongly zoned core and a relatively homogeneous rim; g) and h) BSE images of SHRIMP grains G08-3B and G08-3F respectively showing equant xenotime with oscillatory-zoned cores and compositionally homogenous rim.**

Table 3. SHRIMP U–Pb data for zircon from Abra sandstones and the Tangadee Rhyolite

Analysis spot	*U (ppm)*	*Th (ppm)*	*Th/U*	*f206 (%)*	$^{207}Pb*/^{206}Pb*$	±	$^{206}Pb*/^{238}U$	±	$^{207}Pb*/^{235}U$	±	$^{208}Pb*/^{232}Th$	±	*Disc. (%)*	$^{207}Pb*/^{206}Pb*$ *Age (Ma)*	± *(Ma)*
Abra; detrital grains															
0903B.1-1	423	303	0.74	0.05	0.1230	0.0006	0.3778	0.0066	6.41	0.12	0.1071	0.0020	-3	2000	9
0903E.1-1	134	48	0.37	0.36	0.1194	0.0015	0.3596	0.0070	5.92	0.14	0.0942	0.0035	-2	1948	22
0903E.1-2	73	26	0.37	0.41	0.1197	0.0022	0.3382	0.0091	5.58	0.18	0.0889	0.0048	+4	1951	33
Abra; detrital grains with xenotime overgrowth															
0906Az.2-1	184	210	1.18	0.00	0.1602	0.0014	0.4717	0.0199	10.42	0.45	0.076	0.0040	-1	2457	15
0906Cz.2-1	745	1477	2.05	0.09	0.1081	0.0009	0.2494	0.0097	3.72	0.15	0.062	0.0025	+19	1768	14
Tangadee Rhyolite; xenocrystic grains with xenotime overgrowth															
G08-3A.1-3	198	129	0.67	0.00	0.1114	0.0017	0.324	0.015	4.973	0.239	0.0921	0.0046	+1	1823	28
Tangadee Rhyolite; magmatic grains															
G08-3L.1-1	4478	13069	3.01	25.0	0.0839	0.0133	0.032	0.015	0.373	0.061	0.0098	0.0005	+84	1290	309
G08-3M.1-1	4219	10352	2.53	18.8	0.1406	0.0127	0.025	0.015	0.490	0.051	0.0090	0.0006	+93	2234	156

NOTES: Analysis labels: nnnnA.p–q, where nnnn is the mount number, A is the sample disc on that mount, p is grain number and q is the analysis sequence for the grain
*f*206 is the proportion of common Pb in ^{206}Pb, determined using the measured $^{204}Pb/^{206}Pb$ and a common-Pb composition from the Stacey and Kramers (1975) model at the approximate age of the sample zircon
All Pb isotope data and $t[^{207}Pb*/^{206}Pb*]$ have been corrected for common Pb
Disc. is apparent discordance, as $100(t[^{207}Pb*/^{206}Pb*] - t[^{206}Pb*/^{238}U])/t[^{207}Pb*/^{206}Pb*]$

Xenotime

Xenotime was analysed in two mounts (one 'plug' mount and one grain mount) in one extended analytical session. The primary standard was Xeno-1 ($^{207}Pb/^{206}Pb$ age 997 Ma; $^{206}Pb/^{238}U$ age 994 Ma) and the secondary standards used to monitor matrix effects were MG-1 and BS-1 (see Fletcher et al., 2004). The standards were in a separate mount that was cleaed and Au-coated with the sample mounts.

A ~40 μm Kohler aperture was used, giving ~0.25 nA primary ion beam (O_2^-) and a ~15 × 10 μm analysis spot. The mass resolution was ~5050 and the retardation lens was activated. Seven scans of the mass spectrum were recorded for each analysis.

Eighteen of 23 Xeno-1 analyses give a 1σ external precision for Pb/U of 2.26%, which is propagated to the sample data. The majority of the rejected analyses were of low precision, probably affected by primary beam instability. An insignificantly small correction (-0.03%) was applied to $^{207}Pb/^{206}Pb$ data, with no augmentation of sample precision required by the reproducibility of $^{207}Pb/^{206}Pb$ for the standards. The uncertainty in the mean $^{207}Pb/^{206}Pb$ reference data is insignificant relative to the other sources of uncertainty noted below.

Kiangi Creek Formation sandstone, lying within or above the Abra mineralization (GSWA 149085, 149088, 149089, 149090, 149093)

Eleven in situ analyses (Table 4; Fig. 13) were taken from six xenotime grains (in discs of polished thin sections of sandstone) from the Abra deposit, in mount BR09-06. Three of the xenotimes (0906A.1, 0906E.1, 0906H.1) are outgrowths on visible zircon.

There are two main data clusters. The older group contains seven analyses from four grains (0906A.1 [149085]; 0906G.1 [149088]; 0906H.1 [149090]; 0906M.1 [149085]) that give $^{207}Pb/^{206}Pb$ dates between c. 1966 Ma and c. 1711 Ma. These are likely to be detrital components, though the discordance of some of the data implies additions of younger xenotime.

Grains 0906D.1 [149089] and 0906E.1 [149093] may be a discrete younger component, but only one of these analyses is both concordant and has <1% common ^{206}Pb, and it has a different $^{207}Pb/^{206}Pb$ date (958 ± 35 Ma) than the other three. The discordance (>1σ) of two of the analyses in this young cluster suggests that there may be an additional, still younger, component of xenotime. It is not clear how much of the scatter in this younger group is real and how much reflects analytical limitations, and there is no clearly defined date from the young cluster.

Tangadee Rhyolite (GSWA 149020)

Thirty analyses were obtained from eleven xenotime crystals in grain mount G08-3 (Table 5). Most analyses were placed entirely within visible oscillatory-zoned cores or surrounding unzoned xenotime.

These are low count-rate data, due to low U contents and the small primary ion beam current. Several analyses were aborted due to failure of $^{206}Pb^+$ beam centring, and some of the data were recorded with Pb^+ centring disabled. The precision of some analyses is quite poor due to a combination of the low count rates, possible instabilities in secondary ion beam centring, and possibly also primary beam instability during this session.

Two analyses (G08-3B.1-2 and H.1-4) recorded abnormally low Y_2O^+ count rates and are disregarded, although their $^{207}Pb/^{206}Pb$ data are compatible with the other data. Both of these analyses are from BSE-bright sections of cores, which may represent xenotime of unusual trace-element composition.

Data with >0.2% (or <-0.2%) apparent common ^{206}Pb were not considered for the final age calculations because of the sensitivity of data in this age range to errors in the common-Pb corrections. This has little bearing on interpretations since almost all data with 0.2% – 0.5% apparent common ^{206}Pb have poor precision in $^{207}Pb/^{206}Pb$ because of low U contents (and hence low Pb^+ count rates). Data within ~1σ of concordia have been treated as concordant, even though the low precision means that this includes some data with apparent discordance up to 9%.

There are two distinct age clusters in the concordant data from large grains (Figs 14, 15). Trace element chemistry supports the existence of different generations of xenotime, the older group having higher average Th and lower average U, with average Th/U approximately double that of the younger group. However, there is appreciable overlap between groups.

The older dates all come from visible cores (Fig. 12f–h) in seven of the grains. Their weighted mean $^{207}Pb/^{206}Pb$ date is 1235 ± 19 Ma (MSWD = 0.94; n = 9).

The younger dates all come from outer (rim) portions of four grains and one featureless grain (G08-3E.1-1). The weighted mean $^{207}Pb/^{206}Pb$ date is 1023 ± 40 Ma (MSWD = 1.3; n = 6). The distribution of $^{207}Pb/^{206}Pb$ in the younger group is not symmetric (Fig. 15), with tailing to lower values. Omitting the youngest changes the weighted mean to 1029 ± 28 Ma but reduces MSWD to 0.91, implying over-culling. Mixture modelling (Sambridge and Compston, 1994, incorporated into Isoplot software of Ludwig, 2008) of the concordant data gives a date of 1023 ± 27 Ma for the younger group.

Three analyses that are ~10% discordant (G08-3B.1, F.1, H.1; Table 5) are also from rims and may be part of the younger group. It is possible that all data are offset to lower $^{206}Pb/^{238}U$ by unidentified matrix or calibration effects. If they are included, the weighted mean $^{207}Pb/^{206}Pb$ date of the younger group becomes 1040 ± 32 Ma, but MSWD increases to 1.6. Omitting the oldest and youngest results leaves seven with a weighted mean date of 1034 ± 35 Ma (but MSWD = 0.71, implying over-culling). Since the result depends on data selection, we use an age of 1030 ± 40 Ma that includes the justifiable selections. The fourth discordant analysis (G08-3B.1-3) is from a spot overlapping both core and rim.

The analyses from the xenotime overgrowth on zircon grain G08-3A.1 required very slight corrections for primary beam overlap onto the zircon, which was

Table 4. SHRIMP U–Pb data for Abra xenotime

Analysis spot	*U (ppm)*	*Th (ppm)*	*f206 (%)*	$^{196}[Zr_2O]^+/^{194}[Y_2O]^+$	$^{207}Pb^*/^{206}Pb^*$	±	$^{206}Pb^*/^{238}U$	±	$^{207}Pb^*/^{235}U$	±	$^{208}Pb^*/^{232}Th$	±	*Disc. (%)*	$^{207}Pb^*/^{206}Pb^*$ *Age (Ma)*	± *(Ma)*
Detrital															
0906A.1-1	5465	2614	0.052	0.0021	0.1097	0.0003	0.3205	0.0071	4.846	0.108	0.0451	0.0017	0	1794	4
0906A.1-2	5054	2159	0.041	0.0064	0.1101	0.0003	0.3343	0.0074	5.074	0.113	0.0547	0.0024	-3	1798	6
0906G.1-1	16825	11761	0.004	0.0011	0.1088	0.0001	0.3054	0.0076	4.583	0.114	0.0906	0.0023	3	1780	2
0906G.1-2	15986	12430	0.005	0.0011	0.1075	0.0002	0.2783	0.0077	4.126	0.115	0.0850	0.0038	10	1758	3
0906H.1-1	8380	9245	0.056	0.0013	0.1048	0.0002	0.2637	0.0065	3.811	0.094	0.0679	0.0018	12	1711	4
0906M.1-1	2366	2702	0.010	0.0013	0.1203	0.0004	0.3538	0.0080	5.869	0.134	0.0815	0.0029	0	1961	5
0906M.1-2	2786	2926	0.015	0.0011	0.1207	0.0003	0.3421	0.0076	5.693	0.128	0.0913	0.0022	4	1966	5
Young cluster															
0906E.1-2	2106	2325	0.424	0.0012	0.0710	0.0012	0.1599	0.0037	1.565	0.044	0.0520	0.0013	0	958	35
0906E.1-1	3093	3317	0.534	0.0048	0.0768	0.0009	0.1103	0.0030	1.168	0.035	0.0420	0.0016	40	1105	30
0906D.1-1	673	4288	0.035	0.0011	0.0779	0.0016	0.1323	0.0062	1.422	0.072	0.0411	0.0020	30	1145	41
High common Pb															
0906D.1-2	334	1587	1.156	0.0010	0.0770	0.0030	0.1619	0.0048	1.718	0.079	0.0544	0.0017	14	1121	77

NOTES: The $^{207}Pb^*/^{206}Pb^*$ ages include corrections for zircon overlap for cases with $^{196}[Zr_2O]^+/^{194}[Y_2O]^+>0.0020$. For grain E the zircon composition was assumed to be "typical" Abra detrital age (1800 Ma) and U content (500 ppm)
Analysis labels: nnnnA.p–q, where nnnn is the mount number, A is the sample disc on that mount, p is grain number and q is the analysis sequence for the grain
*f*206 is the proportion of common Pb in ^{206}Pb, determined using the measured $^{204}Pb/^{206}Pb$ and a common-Pb composition from the Stacey and Kramers (1975) model at the approximate age of the sample zircon
All Pb isotope data and $t[^{207}Pb^*/^{206}Pb^*]$ have been corrected for common Pb
Disc. is apparent discordance, as $100(t[^{207}Pb^*/^{206}Pb^*] - t[^{206}Pb^*/^{238}U])/t[^{207}Pb^*/^{206}Pb^*]$

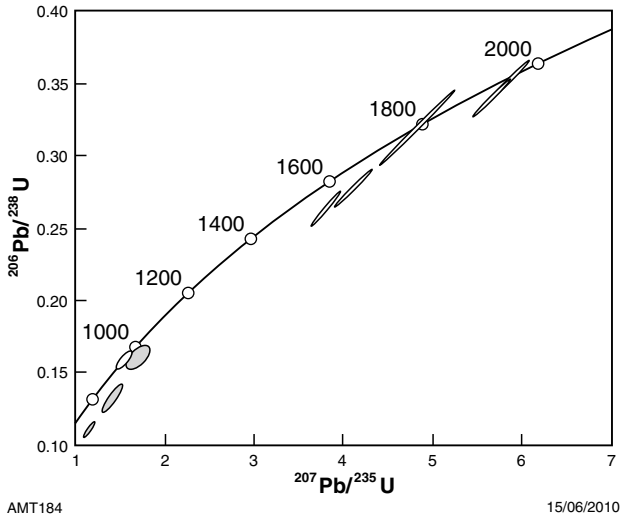

Figure 13. Concordia plot of the U–Pb data for Abra xenotimes exposed in thin sections (mount 09-06; Table 4). Shaded points are >5% discordant or have >1% common ^{206}Pb. Ellipses are 1σ.

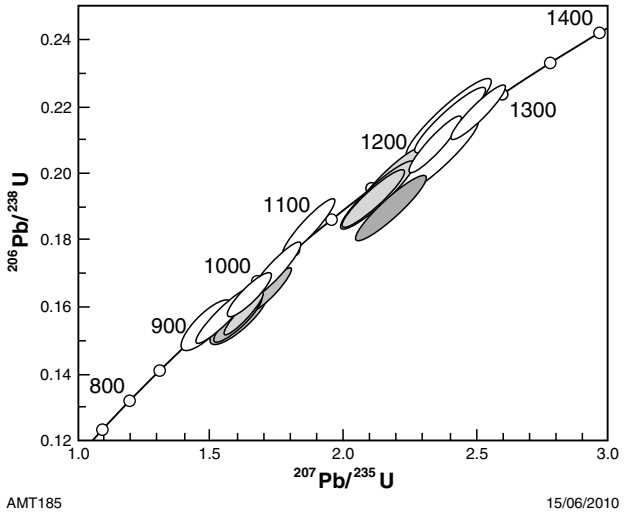

Figure 14. Concordia plot of the U–Pb data for Tangadee Rhyolite xenotime (mount G08-3; Table 5). Dark shaded analyses are ≥10% discordant; light shaded are >5% nominal discordant but within ~1σ of concordance. Ellipses are 1σ.

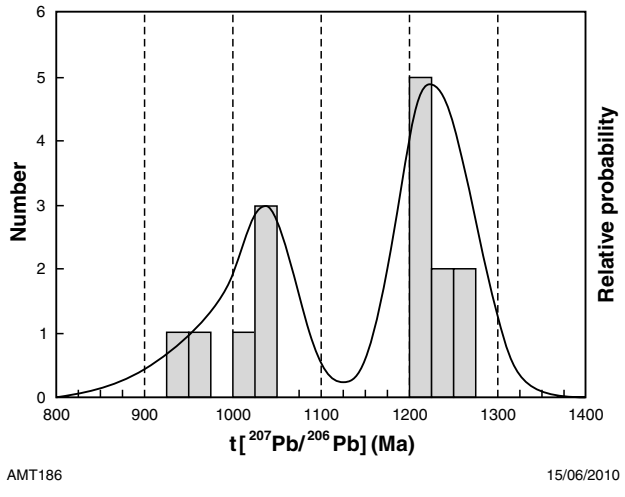

Figure 15. Probability density diagram of $^{207}Pb/^{206}Pb$ dates for the two principal groups of xenotime data from Tangadee Rhyolite, (mount G08-3; Table 5).

Table 5. SHRIMP U–Pb data for Tangadee Rhyolite xenotime

Analysis spot	*U (ppm)*	*Th (ppm)*	*Th/U*	*f206 (%)*	$^{207}Pb^*/^{206}Pb^*$	±	$^{206}Pb^*/^{238}U$	±	$^{207}Pb^*/^{235}U$	±	$^{208}Pb^*/^{232}Th$	±	*Disc. (%)*	$^{207}Pb^*/^{206}Pb^*$ *Age (Ma)*	± *(Ma)*
Young cluster															
G08-3C.1-1	541	1752	3.2	-0.070	0.0702	0.0019	0.1544	0.0050	1.494	0.061	0.0488	0.0017	1	933	56
G08-3C.1-2	575	1572	2.7	-0.124	0.0714	0.0013	0.1562	0.0048	1.537	0.053	0.0500	0.0021	3	968	36
G08-3E.1-1	752	1686	2.2	-0.095	0.0734	0.0011	0.1625	0.0047	1.645	0.053	0.0522	0.0016	5	1025	30
G08-3K.1-1	603	3061	5.1	0.093	0.0740	0.0011	0.1837	0.0055	1.874	0.061	0.0562	0.0017	-4	1041	30
G08-3I.1-1	595	3284	5.5	0.151	0.0741	0.0012	0.1592	0.0048	1.627	0.055	0.0502	0.0016	9	1045	33
G08-3G.1-1	575	3166	5.5	0.055	0.0743	0.0011	0.1714	0.0053	1.755	0.059	0.0526	0.0017	3	1049	30
Old cluster															
G08-3B.1-4	757	5433	7.2	-0.073	0.0803	0.0010	0.1918	0.0055	2.124	0.066	0.0589	0.0018	6	1205	24
G08-3G.1-2	317	4432	14.0	-0.078	0.0805	0.0014	0.1939	0.0071	2.152	0.087	0.0605	0.0023	6	1209	35
G08-3F.1-3	253	985	3.9	0.105	0.0808	0.0018	0.2155	0.0084	2.399	0.104	0.0667	0.0027	-4	1215	43
G08-3D.1-2	549	5497	10.0	0.094	0.0808	0.0011	0.1921	0.0059	2.140	0.072	0.0598	0.0019	7	1217	28
G08-3K.1-2	402	4738	11.8	0.171	0.0811	0.0014	0.2149	0.0074	2.403	0.091	0.0654	0.0024	-2	1224	34
G08-3I.1-2	164	643	3.9	0.000	0.0813	0.0018	0.2020	0.0089	2.263	0.109	0.0639	0.0030	3	1228	43
G08-3G.1-3	595	4286	7.2	-0.041	0.0818	0.0010	0.2079	0.0065	2.344	0.077	0.0624	0.0020	2	1240	24
G08-3H.1-2	265	2715	10.3	0.087	0.0832	0.0016	0.2062	0.0079	2.366	0.099	0.0622	0.0025	5	1274	37
G08-3K.1-3	969	8426	8.7	0.130	0.0832	0.0009	0.2176	0.0060	2.496	0.073	0.0650	0.0018	0	1274	21
≥10% discordant															
G08-3B.1-3	583	7041	12.1	-0.046	0.0843	0.0011	0.1892	0.0058	2.198	0.073	0.0573	0.0018	14	1299	25
G08-3B.1-1	586	3404	5.8	-0.066	0.0744	0.0012	0.1565	0.0049	1.606	0.056	0.0484	0.0016	11	1052	33
G08-3F.1-1	680	3877	5.7	0.000	0.0760	0.0010	0.1645	0.0049	1.724	0.055	0.0512	0.0016	10	1095	25
G08-3H.1-1	188	243	1.3	0.000	0.0745	0.0018	0.1591	0.0070	1.634	0.080	0.0511	0.0025	10	1055	49
High or anomalous $^{204}Pb^+$															
G08-3I.1-3	182	1665	9.1	0.241	0.0785	0.0021	0.2000	0.0086	2.166	0.108	0.0609	0.0027	-1	1160	54
G08-3D.1-1	523	3310	6.3	0.256	0.0734	0.0015	0.1681	0.0054	1.701	0.064	0.0529	0.0018	2	1025	42
G08-3J.1-1b	124	188	1.5	0.266	0.0696	0.0032	0.1512	0.0081	1.451	0.098	0.0462	0.0028	1	916	93
G08-3H.1-3	217	913	4.2	-0.504	0.0903	0.0027	0.2014	0.0087	2.508	0.128	0.0635	0.0029	17	1432	57
G08-3F.1-2x	330	1525	4.6	1.051	0.0800	0.0037	0.2089	0.0076	2.305	0.128	0.0462	0.0019	-2	1198	90
Overgrowth on zircon															
G08-3A.1-1	408	2427	6.0	0.733	0.0767	0.0036	0.1702	0.0058	1.800	0.099	0.0453	0.0029	9	1114	94
G08-3A.1-1b	499	3971	7.9	0.966	0.0739	0.0036	0.1733	0.0054	1.766	0.096	0.0357	0.0013	1	1039	99
G08-3A.1-2	153	817	5.3	0.449	0.0708	0.0042	0.1594	0.0079	1.556	0.114	0.0504	0.0027	0	952	120
G08-3A.1-2b	148	863	5.8	0.224	0.0774	0.0028	0.1692	0.0076	1.806	0.101	0.0515	0.0030	11	1132	73
Low Y_2O+ counts															
G08-3B.1-2	1333	6144	4.6	0.056	0.0830	0.0008	0.2127	0.0060	2.435	0.073	0.0625	0.0019	2	1270	20
G08-3H.1-4	1219	6781	5.6	0.648	0.0784	0.0017	0.1432	0.0041	1.548	0.054	0.0192	0.0020	26	1158	44

NOTES: $^{196}[Zr_2O]^+/^{194}[Y_2O]^+<0.0020$ for the overgrowths on zircon; no corrections required

Analysis labels: nnnnA.p–q, where nnnn is the mount number, A is the sample disc on that mount, p is grain number and q is the analysis sequence for the grain

*f*206 is the proportion of common Pb in ^{206}Pb, determined using the measured $^{204}Pb/^{206}Pb$ and a common-Pb composition from the Stacey and Kramers (1975) model at the approximate age of the sample zircon

All Pb isotope data and $t[^{207}Pb^*/^{206}Pb^*]$ have been corrected for common Pb

Disc. is apparent discordance, as $100(t[^{207}Pb^*/^{206}Pb^*] - t[^{206}Pb^*/^{238}U])/t[^{207}Pb^*/^{206}Pb^*]$

monitored by Zr_2O^+/Y_2O^+. These corrections have been applied to the data in Table 5. Although less precise, these data are clearly consistent with results from the outer areas of the discrete grains in the rhyolite.

Monazite

Monazite was analysed in two 'plug' mounts: BR09-04 and BR09-05. The primary Pb/U and Pb/Th standard was 'French' ($^{206}Pb/^{238}U$ age 514 Ma; $^{208}Pb/^{232}Th$ age 504 Ma) and the secondary standards used to monitor matrix effects were z2908, z2234 and PD-95 (see Fletcher et al., 2010). Z2908 was also the main monitor of mass fractionation. The standards were in a separate mount that was cleaned and Au-coated with the sample mounts.

Data were acquired in two sessions. In the first, grains on both mounts were analysed using a 50 µm Kohler aperture, ~0.45 nA primary ion beam (O_2^-) and a ~15 µm analysis spot. The mass resolution was ~5050. In the second session only the grain cluster 0904K was analysed, using a ~30 µm Kohler aperture, ~0.35 nA primary ion beam and ~12 µm spot. The mass resolution was ~5150. In both sessions the retardation lens was activated, and seven scans of the mass spectrum were recorded for each analysis.

The 1σ external precision for Pb/U was of 3.2% (n = 9 of 12) and 2.7% (n = 7 of 9) for the two sessions. Corresponding figures for Pb/Th were 2.6% and 3.2%. An insignificantly small fractionation correction (0.02%) was applied to $^{207}Pb/^{206}Pb$ data in the first session, with no augmentation of sample precision required by the reproducibility of $^{207}Pb/^{206}Pb$ for the standards. In the second session the correction was 0.21% and a 1σ external precision of 0.16% was propagated. The uncertainty in the mean $^{207}Pb/^{206}Pb$ reference data is insignificant relative to the other sources of uncertainty in the sample data.

Inclusions in detrital quartz (GSWA 149085, 149088, 149089, 149090)

Eighteen analyses were obtained from 14 inclusions (Table 6). Two of these (from the same grain) had low $CePO_2^+$ counts and were not considered for chronology. The remainder, including five with high common Pb, give detrital $^{207}Pb/^{206}Pb$ dates. For concordant data with <1% common ^{206}Pb, the $^{207}Pb/^{206}Pb$ dates range from c. 1675 Ma to c. 1820 Ma, with a possible peak at c. 1780 Ma (Fig. 19).

Hydrothermal monazite (GSWA149085, 149086, 149093)

Thirty-three analyses were obtained from 4 grains (Table 7), about half of them from the cluster of grains in disc 0904K (from GSWA 149086). These are the largest of the hydrothermal grains and have the lowest proportions of common Pb. The actual levels of common Pb are more uniform in these samples than the f206 in Table 7 would suggest, the variation being due more to variations in radiogenic Pb (because of variations in U). One analysis had a very low $CePO_2^+$ count rate; this has been disregarded.

Twelve analyses, all from 09-04K (149086), have <1% common ^{206}Pb and define a single $^{207}Pb/^{206}Pb$ age component. Two others are >5% discordant but barely more than 1σ from concordia (Fig. 17). These fourteen analyses have a weighted mean of 1382 ± 15 Ma (MSWD = 0.84). If the two marginally discordant analyses are excluded, the weighted mean $^{207}Pb/^{206}Pb$ date becomes 1388 ± 16 Ma (MSWD = 0.67).

Two concordant analyses (0904K.1-2, 1-8) with <1% common Pb are distinct old outliers from the c. 1380 Ma main population of hydrothermal monazite (1462 ± 22 Ma and 1484 ± 33 Ma, respectively). These analyses imply that some monazite grew at c. 1470 Ma in the sandstones in response to an earlier event but, if so, their close association with the rest of the 0904K grains (which all appear to have the younger age) is surprising.

Although the data with >1% common ^{206}Pb cannot be used to improve the precision of the date, when all the data are plotted together they lie close (MSWD = 1.3) to a single isochron (common Pb–radiogenic Pb mixing trend; Fig. 18), implying that most of the monazite formed in a single event. However, the isochron projects above the coordinates of both Abra galena Pb and any reasonable model common-Pb composition. There are no potential analytical problems that could explain this anomaly. A further complication arises if isochron dates are determined. The date from the entire dataset (Fig. 18) is almost identical to that determined directly from $^{207}Pb/^{206}Pb$ for the analyses with low common Pb. However, if the two apparent old outliers are omitted, the isochron result is appreciably lower, at c. 1370 Ma.

Because the calculated date is dependent on data selection and data treatment, we use a date of 1385 ± 20 Ma that includes the results of all justifiable options.

Discussion

Zircon grains in sandstones from the Abra deposit give dates between c. 2450 Ma and c. 1950 Ma. These dates are similar to those from detrital zircons elsewhere from the Edmund Group (Martin et al., 2008). A single analysis of a xenocrystic zircon from the Tangadee Rhyolite gives a date of 1823 ± 28 Ma.

Detrital xenotime and inclusions of xenotime in detrital quartz grains from sandstones at Abra give dates between 1966 Ma and 1711 Ma. Xenotime overgrowths on detrital zircon from these sandstones are either discordant or have high common Pb and are therefore not reliable for age determination. A single low common-Pb concordant analysis of a xenotime overgrowth gave a date of 958 ± 35 Ma, the meaning of which is uncertain. It may have formed during the latter stages of the 1030–950 Ma Edmundian Orogeny (Martin et al., 2005; Sheppard et al., 2007; Johnson et al., 2009). However, this also broadly corresponds with the age of the younger population of xenotime from the Tangdadee Rhyolite (see below). In the Gascoyne Province, c. 950 Ma corresponds to the timing of emplacement of rare-element pegmatites (Sheppard et al., 2007).

Table 6. SHRIMP U–Pb data for Abra monazite inclusions

Analysis spot	*U (ppm)*	*Th (ppm)*	*Th/U*	*f206 (%)*	$^{207}Pb^*/^{206}Pb^*$	±	$^{206}Pb^*/^{238}U$	±	$^{207}Pb^*/^{235}U$	±	$^{208}Pb^*/^{232}Th$	±	*Disc. (%)*	$^{207}Pb^*/^{206}Pb^*$ *Age (Ma)*	± *(Ma)*
Main group															
0904J.1-1	1610	58583	36	0.022	0.1102	0.0005	0.310	0.011	4.71	0.16	0.091	0.011	4	1803	8
0904I.1-1	1033	46017	45	0.320	0.1069	0.0009	0.300	0.010	4.42	0.15	0.096	0.010	3	1747	15
0905D.1-1	621	47501	77	0.090	0.1091	0.0008	0.320	0.011	4.81	0.17	0.098	0.011	0	1785	13
0904F.1-1	923	35806	39	0.010	0.1094	0.0004	0.322	0.011	4.86	0.17	0.095	0.011	-1	1790	7
0905A.1-1	5738	46470	8	0.011	0.1090	0.0002	0.321	0.011	4.83	0.16	0.094	0.011	-1	1783	3
0904M.1-1	3193	95014	30	0.030	0.1090	0.0004	0.322	0.011	4.83	0.16	0.096	0.011	-1	1782	7
0905I.1-1	3435	44231	13	0.173	0.1111	0.0003	0.330	0.011	5.05	0.17	0.098	0.011	-1	1818	5
0905H.1-1	10633	57060	5	0.011	0.1029	0.0002	0.305	0.010	4.32	0.15	0.091	0.010	-2	1677	3
0905L.1-1	617	49555	80	0.123	0.1089	0.0008	0.326	0.011	4.90	0.16	0.101	0.011	-2	1780	13
0904D.1-1	2341	46486	20	0.036	0.1087	0.0003	0.334	0.011	5.01	0.16	0.099	0.011	-4	1779	5
0905G.1-1	4321	35032	8	0.052	0.1028	0.0002	0.314	0.010	4.46	0.15	0.078	0.010	-5	1676	4
High common Pb															
0904E.1-3	385	33527	87	2.233	0.1048	0.0016	0.350	0.019	5.05	0.28	0.091	0.019	-13	1710	29
0904E.1-1	137	28265	206	3.942	0.1167	0.0045	0.330	0.014	5.30	0.30	0.083	0.014	4	1907	69
0904H.1-1	187	31753	170	4.085	0.1008	0.0032	0.315	0.012	4.38	0.22	0.063	0.012	-8	1639	60
0904E.1-2	405	23933	59	4.877	0.1016	0.0048	0.089	0.013	1.24	0.19	0.064	0.013	67	1654	88
0904E.1-4	143	31054	218	5.364	0.1034	0.0039	0.525	0.029	7.49	0.50	0.081	0.029	-61	1686	69
Low $CePO_2^+$															
0904A.1-1	24723	16017	0.6	-0.018	0.1090	0.0004	0.210	0.007	3.16	0.10	0.080	0.007	31	1782	6
0904A.1-2	17501	6176	0.4	-0.022	0.1085	0.0008	0.216	0.007	3.23	0.11	0.085	0.007	29	1774	13

NOTES: Analysis labels: nnnnA.p–q, where nnnn is the mount number, A is the sample disc on that mount, p is grain number and q is the analysis sequence for the grain
*f*206 is the proportion of common Pb in ^{206}Pb, determined using the measured $^{204}Pb/^{206}Pb$ and a common-Pb composition from the Stacey and Kramers (1975) model at the approximate age of the sample zircon
All Pb isotope data and $t[^{207}Pb^*/^{206}Pb^*]$ have been corrected for common Pb
Disc. is apparent discordance, as $100(t[^{207}Pb^*/^{206}Pb^*] - t[^{206}Pb^*/^{238}U])/t[^{207}Pb^*/^{206}Pb^*]$

Table 7. SHRIMP U–Pb data for Abra hydrothermal monazite

Analysis spot	U (ppm)	Th (ppm)	Th/U	f206 (%)	$^{207}Pb^*/^{206}Pb^*$	±	$^{206}Pb^*/^{238}U$	±	$^{207}Pb^*/^{235}U$	±	$^{208}Pb^*/^{232}Th$	±	Disc. (%)	$^{207}Pb^*/^{206}Pb^*$ Age (Ma)	± (Ma)
Main group															
0904K.1-9	228	2519	11.0	0.52	0.0861	0.0018	0.233	0.007	2.76	0.10	0.0601	0.0069	-1	1341	40
0901K.1-16	199	573	2.9	0.49	0.0864	0.0019	0.236	0.007	2.82	0.10	0.0730	0.0068	-1	1348	42
0904K.1-5	234	1294	5.5	0.30	0.0871	0.0011	0.238	0.008	2.86	0.10	0.0591	0.0078	-1	1363	25
0904K.1-12	181	2821	15.6	0.76	0.0871	0.0023	0.229	0.007	2.75	0.11	0.0561	0.0067	2	1363	52
0901K.1-17	272	782	2.9	0.34	0.0875	0.0012	0.245	0.008	2.96	0.10	0.0634	0.0078	-3	1371	26
0904K.1-13	351	578	1.6	0.42	0.0878	0.0017	0.238	0.007	2.89	0.10	0.0627	0.0072	0	1379	38
0901K.1-18	181	666	3.7	0.51	0.0880	0.0017	0.245	0.007	2.97	0.10	0.0536	0.0073	-2	1383	36
0904K.1-1	291	331	1.1	0.30	0.0881	0.0012	0.226	0.006	2.74	0.09	0.0541	0.0065	5	1384	26
0904K.1-20	226	2857	12.7	0.42	0.0886	0.0017	0.235	0.007	2.87	0.10	0.0600	0.0070	3	1395	37
0904K.1-6	200	1982	9.9	0.14	0.0889	0.0011	0.236	0.008	2.90	0.10	0.0559	0.0078	2	1402	24
0904K.1-4	148	1414	9.5	0.69	0.0894	0.0018	0.230	0.008	2.84	0.12	0.0644	0.0083	5	1412	38
0904K.1-10	335	982	2.9	0.17	0.0895	0.0008	0.248	0.007	3.06	0.09	0.0590	0.0070	-1	1415	17
Old outliers															
0904K.1-2	170	2694	15.8	-0.02	0.0917	0.0011	0.248	0.008	3.13	0.11	0.0593	0.0083	2	1462	22
0904K.1-8	147	1538	10.5	0.46	0.0928	0.0016	0.252	0.007	3.22	0.11	0.0662	0.0074	3	1484	33
Discordant															
0904K.1-3	491	736	1.5	0.13	0.0876	0.0010	0.193	0.007	2.33	0.09	0.0502	0.0069	17	1373	22
0904K.1-1	342	1300	3.8	0.11	0.0864	0.0009	0.216	0.007	2.58	0.09	0.0533	0.0070	6	1348	20
0904K.1-11	173	1001	5.8	0.48	0.0883	0.0015	0.262	0.008	3.18	0.11	0.0726	0.0077	-8	1389	32
High common Pb															
0904K.1-19	175	3269	19	1.02	0.0884	0.0024	0.243	0.007	2.95	0.12	0.0594	0.0073	-1	1390	52
0901K.1-15	131	1043	8	1.03	0.0909	0.0029	0.240	0.007	3.01	0.13	0.0563	0.0075	4	1444	61
0904B.1-1	119	5304	45	4.48	0.1006	0.0044	0.250	0.008	3.47	0.19	0.0722	0.0084	12	1636	82
0904B.1-2	179	6077	34	4.74	0.0971	0.0072	0.240	0.009	3.21	0.27	0.0677	0.0090	12	1568	138
0904B.1-6	107	7066	66	4.93	0.1118	0.0094	0.221	0.008	3.41	0.31	0.0583	0.0076	30	1830	152
0904G.1-1	76	4603	60	4.93	0.0937	0.0175	0.205	0.007	2.65	0.50	0.0679	0.0073	20	1503	353
0904B.1-4	108	7622	71	5.08	0.1071	0.0103	0.224	0.009	3.31	0.35	0.0606	0.0092	26	1751	175
0904B.1-5	109	6508	59	5.10	0.1031	0.0056	0.228	0.009	3.24	0.22	0.0586	0.0088	21	1681	101
0904B.1-3	144	5956	41	5.16	0.0922	0.0052	0.257	0.009	3.27	0.22	0.0729	0.0086	0	1471	107
0904G.1-2	57	5313	93	6.19	0.1131	0.0113	0.216	0.010	3.38	0.37	0.0670	0.0103	32	1851	181
0904G.1-4	52	4365	84	10.32	0.0836	0.0148	0.191	0.010	2.20	0.41	0.0650	0.0096	12	1283	345
0904C.1-2	24	3310	136	12.17	0.2055	0.0388	0.134	0.007	3.81	0.75	0.0586	0.0071	72	2871	307
0904G.1-3	29	4359	148	13.91	0.1300	0.0214	0.226	0.014	4.05	0.71	0.0697	0.0139	37	2098	289
0904C.2-3	29	4749	166	23.75	0.1810	0.0702	0.164	0.021	4.10	1.67	0.0600	0.0206	63	2662	643
0904C.2-2	14	5217	374	25.58	0.2019	0.0738	0.287	0.024	7.98	3.00	0.0631	0.0236	43	2841	595
0904C.2-1	10	2901	284	32.81	0.2546	0.1128	0.270	0.033	9.47	4.36	0.0648	0.0332	52	3214	700
Low $CePO_2^+$															
0904K.-14	185	1212	7	3.05	0.0802	0.0053	0.248	0.008	2.74	0.20	0.0556	0.0077	-19	1203	130

NOTES: Analysis labels: nnnnA.p–q, where nnnn is the mount number, A is the sample disc on that mount, p is grain number and q is the analysis sequence for the grain
*f*206 is the proportion of common Pb in ^{206}Pb, determined using the measured $^{204}Pb/^{206}Pb$ and a common-Pb composition from the Stacey and Kramers (1975) model at the approximate age of the sample zircon
All Pb isotope data and $t[^{207}Pb^*/^{206}Pb^*]$ have been corrected for common Pb
Disc. is apparent discordance, as $100(t[^{207}Pb^*/^{206}Pb^*] - t[^{206}Pb^*/^{238}U])/t[^{207}Pb^*/^{206}Pb^*]$

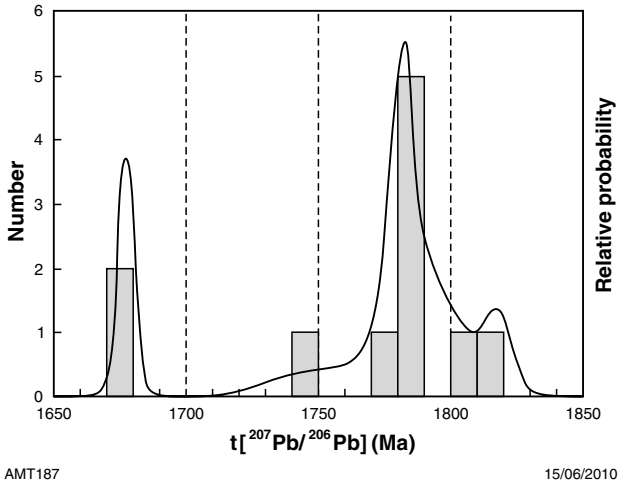

Figure 16. Probability density diagram of $^{207}Pb/^{206}Pb$ dates for Abra monazite inclusions (mounts 09-04 and 09-05; Table 6).

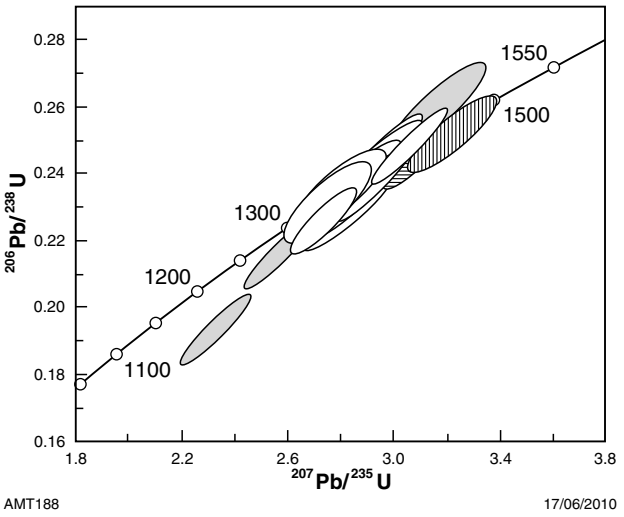

Figure 17. Concordia plot of the U–Pb data for Abra hydrothermal monazite with <1% common ^{206}Pb (mount 09-04; Table 5). Shaded analyses are ≥5% discordant, hatched are concordant old outliers. Ellipses are 1σ.

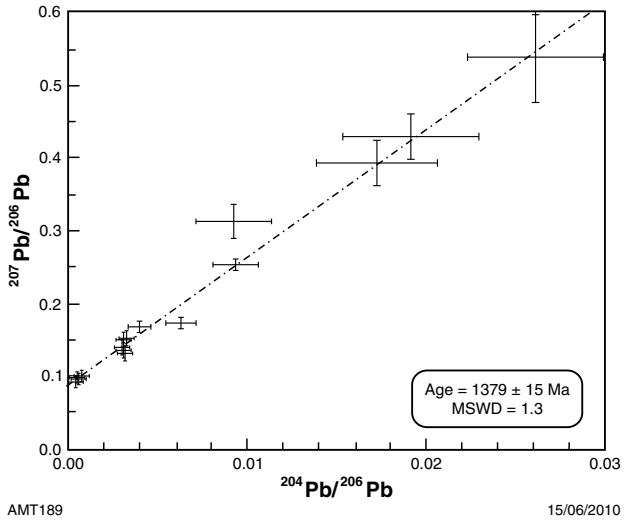

Figure 18. Pb/Pb (inverse) isochron plot for Abra hydrothermal monazite (mount 09-04; Table 7). Precision bars are 1σ.

The c. 1385 Ma monazite date for the Abra mineralization and the c. 1235 and c. 1030 Ma xenotime dates from the associated Tangadee Rhyolite are significantly younger than the depositional age of the Edmund Group. Moreover, if the core of the dated xenotime from the Tangadee Rhyolite is magmatic it implies that the rhyolite emplacement was unrelated to the Abra mineralization event. These findings contradict previous interpretations for the timing of the Abra mineralization and emplacement of the Tangadee Rhyolite and are discussed below.

Abra mineralization (c. 1385 Ma)

Monazite grains from sandstones in and around the Abra polymetallic deposit are inclusions within detrital quartz and irregular hydrothermal aggregates in the chlorite–carbonate matrix. In situ SHRIMP geochronology of the monazite inclusions yields dates between c. 1820 Ma and c. 1680 Ma, consistent with a detrital origin for these grains.

The hydrothermal monazite yielded a date of 1385 ± 20 Ma, which is consistent with available geochronological constraints for mineralization. Several older monazite grains (1484 ± 33 Ma and 1462 ± 22 Ma) may have formed during emplacement of the c. 1.46 Ga mafic igneous event in the Edmund Group. The growth of monazite at this time indicates that the sandstones must be older than 1.46 Ga, consistent with the succession belonging to the Edmund Group.

The monazite date of c. 1385 Ma from mineralized sandstone within the Red Zone of the Abra ore body is younger than the younger limit age for the Edmund Group host rocks which is currently fixed by the c. 1465 Ma age of the intrusive Narimbunna Dolerite and by c. 1460 Ma felsic volcanic rocks in the Ullawarra Formation. One interpretation of this date is that most if not all of the Abra mineralization occurred c. 95 Ma after the Edmund Group was deposited. This interpretation is difficult to reconcile with the stratigraphic setting of the mineralization, which suggests it was coeval with deposition of the lower to middle Edmund Group (Vogt and Stumpfl, 1987; Collins and McDonald, 1994; Vogt, 1995; Pirajno et al., 2009; Thorne et al., 2009). The interpretation of these workers is based largely on the nature of the upper contact of the mineralization, which terminates against a syndepositional erosion surface, considered to mark the top of either the Irregully (Gap Well) Formation (Collins and McDonald, 1994) or the top of a conglomeratic unit within the lower Kiangi Creek (West Creek) Formation (Vogt, 1995; Pirajno et al., 2009; Thorne et al., 2009).

Two possible explanations for reconciling the age data with the stratigraphic relationships have been considered:

1) The c. 1385 Ma monazite date equates to the timing of the main Abra mineralization event. The sharp upper contact of the main orebody may have been caused by the relatively impermeable marine and fan-delta facies acting as a seal and trapping the mineralizing fluid system in the more permeable fluvial and carbonate-rich rocks below.
2) The monazite date records a younger mineralization event during which there was remobilization of sulfide and gangue minerals from an older, synsedimentary orebody. This younger hydrothermal event could be responsible for the thin veins of barite, chalcopyrite, dolomite, and galena found in the Kiangi Creek (West Creek) Formation marine and fan-delta facies overlying the major mineralization.

On the available evidence it is not possible to say which of the two explanations is correct and further geochronological studies of the mineralization are needed to resolve this problem.

c. 1385 Ma events in the Capricorn Orogen

The c. 1385 Ma monazite age for the Abra mineralization does not match any previously known event in the Capricorn Orogen. It post-dates the Edmund Group, but its timing in relation to the deposition of the overlying Collier Group is not known with certainty because of the poor age constraints on the latter.

Few other c. 1385 Ma events are recorded elsewhere in Western Australia. Smithies et al. (2009) presented data from the Wirku Metamorphics in the west Musgrave Province that suggest that sediments were deposited over a wide region between 1360 and 1307 Ma, prior to and coincident with intrusion by granites of the 1336–1293 Ma Wankanki Supersuite.

Tangadee Rhyolite (c. 1235 Ma and c. 1030 Ma)

Euhedral xenotime extracted from the Tangadee Rhyolite (GSWA 149020) yields two main age components. Oscillatory-zoned cores yield a $^{207}Pb/^{206}Pb$ date of 1235 ± 19 Ma, whereas unzoned rims yield a $^{207}Pb/^{206}Pb$ date of 1030 ± 40 Ma. The strong oscillatory zoning in the cores as well as the lack of inclusions suggests a magmatic origin for this generation of xenotime. Although the outer xenotime typically has planar faces, rims are locally intergrown with grains of K-feldspar, kaolinite, rutile, and a tin oxide mineral, possibly cassiterite. In places, the oscillatory zoning is disrupted and mottled, possibly suggesting that xenotime cores were partly dissolved and reprecipitated during a younger event.

There are several possible explanations for the age distribution of the xenotime in the Tangadee Rhyolite (assuming that the rhyolite is an extrusive rather than low-level intrusive unit):

1) The oscillatory-zoned cores are xenocrystic, and therefore do not represent the age of the rhyolite, whereas the rims are magmatic. This implies an extrusion age of c. 1030 Ma, which suggests that the associated sedimentary sequences are younger than either the Edmund Group (<1620 Ma to 1465 Ma) or the Collier Group (<1465 Ma and >1070 Ma).

2) The cores formed during crystallization of the rhyolite, whereas the younger rims formed during a later hydrothermal event (c. 1030 Ma). This would suggest that the rhyolite was extruded at c. 1235 Ma, and that the surrounding sedimentary rocks are much younger than the Edmund Group (<1620 Ma to >1465 Ma).
3) Both generations of xenotime formed long after deposition during two different hydrothermal events. This scenario would suggest that the depositional age of the Tangadee Rhyolite is somewhere between c. 1640 Ma, from the youngest xenocrystic zircons, and c. 1235 Ma, from the oldest hydrothermal xenotime.

The first scenario is unlikely because it suggests that the sedimentary rocks into which the Tangadee Rhyolite was extruded are younger than either the Edmund Group or overlying Collier Group. The second scenario probably best explains the available data, but would indicate that the surrounding successions are part of the basal Collier Group or a succession deposited between the Edmund and Collier Groups. The third alternative is consistent with geological mapping, which places the rhyolite within the Edmund Group. However, this requires the growth of xenotime in the matrix of the rhyolite long after extrusion, with the development of equant, inclusion-free xenotime with strong oscillatory-zoned cores.

The c. 1235 Ma date from the core of xenotime in the Tangadee Rhyolite is younger than the depositional age of the Edmund Group, whereas the c. 1030 Ma date from the rim of the same xenotime grain is both younger than the overlying Collier Group and the 1070 Ma dolerite of the Warakurna Large Igneous Province (Wingate et al., 2004; Morris and Pirajno, 2005). Of the two xenotime dates, the c. 1030 Ma date from the rim is the more straightforward to interpret and probably results from growth during a late-stage hydrothermal event. The date is within error of the Rb–Sr isochron of 1098 ± 42 Ma obtained by Gee et al. (1976) from the Tangadee Rhyolite, who also argued that this dated a post-emplacement alteration event.

Although the zoned, euhedral structure of the c. 1235 Ma xenotime core argues strongly for a magmatic origin, this interpretation is difficult to reconcile with the known geological relationships of the Tangadee Rhyolite. The presence of rhyolite pebbles in the overlying sedimentary succession and the occurrence of syndepositional felsic volcaniclastic facies at the same stratigraphic level can be used to rule out a later intrusive origin for the Tangadee Rhyolite. If it is accepted that the Tangadee Rhyolite is extrusive, then the associated sedimentary succession, previously considered to form part of the Edmund Group, must belong instead to a younger stratigraphic unit, such as the Collier Group. Although such an explanation is possible, it is considered unlikely, based on the geological setting of the rhyolite and its associated sedimentary succession, which are preserved in the core of a partially fault-bound anticline less than 100 m above the contact with the underlying 1797 Ma Moorarie Supersuite granite. Although the discontinuous nature of the outcrop precludes absolute certainty, the host rocks of the Tangadee Rhyolite are apparently overlain by units of the middle to upper Edmund Group. For the Tangadee Rhyolite and its host rocks to be younger than the Edmund Group would require the presence of concealed faulting or a very localized, concealed unconformity to separate these stratigraphic units.

A c. 1235 Ma age for the extrusive Tangadee Rhyolite also has to be reconciled with the work of Collins and McDonald (1994), who recorded the presence of rhyolite pebbles in conglomerate from the lower part of the Kiangi Creek Formation (unit WC1 of Vogt, 1995). The nature of the sedimentary facies, including paleocurrent trends, in the lower part of the Kiangi Creek Formation around Abra also closely matches that of the host rocks of the Tangadee Rhyolite, and is an important factor in their correlation (Vogt, 1995; Thorne et al., 2009).

c. 1235 and c. 1040 Ma events in the Capricorn Orogen

The date of c. 1235 Ma for xenotime cores from the Tangadee Rhyolite could relate to the c. 1280–1250 Ma event recognized by Johnson et al. (2009) in garnet–staurolite schists of the Leake Spring Metamorphics (Gascoyne Province). Monazite parallel to relict, folded S_1 fabrics within garnet and staurolite porphyroblasts give consistent dates of c. 1280 Ma, whereas those within the main S_2 fabric give dates of c. 1250 Ma.

The c. 1040 Ma date from the xenotime rims in the Tangadee Rhyolite might be associated with the same alteration event as the Rb–Sr isochron date of 1098 ± 42 Ma obtained by Gee et al. (1976) from the same unit. The xenotime rim date is c. 30 Ma older than the 1078–1070 Ma dolerite sills of the Warakurna Large Igneous Province (Wingate et al., 2004; Morris and Pirajno, 2005) that intrude the Edmund and Collier Groups throughout the Capricorn Orogen, but is close to the 1030 Ma date that marks the start of the Edmundian Orogeny (Johnson et al., 2009).

Conclusions

In situ SHRIMP geochronology of hydrothermal monazite from the Abra deposit suggests that a mineralization event occurred at c. 1385 Ma. The presence of metamorphic and/or hydrothermal monazite in sandstones from Abra that grew at c. 1465 Ma indicates that the host rocks to mineralization were older than 1465 Ma and therefore belong to the Edmund Group. SHRIMP geochronology of xenotime extracted from the Tangadee Rhyolite indicates a possible eruption age of c. 1235 Ma and a later hydrothermal overprint at c. 1030 Ma, although this contradicts evidence from the geological setting of the rhyolite, and other interpretations are possible.

Acknowledgements

U–Pb measurements were conducted using the SHRIMP ion microprobes at the John de Laeter Centre of Mass Spectrometry at Curtin University of Technology, Perth, Western Australia.

References

Abra Mining Ltd, 2010, Abra Mining Ltd, Perth, viewed 2010, <http://www.abramining.com.au/>.

Austen, S 2007, Isotopic and thermal constraints on the origin and formation of the Abra polymetallic deposit, Jillawarra Sub-basin, Western Australia: University of Southampton, United Kingdom, School of Ocean and Earth Science, MSc thesis (unpublished).

Boddington, TDM 1990, Abra lead–silver–copper–gold deposit, *in* Mineral deposits of Australia and Papua New Guinea *edited by* FE Hughes: Australasian Institute of Mining and Metallurgy, Monograph 14, p. 659–664.

Brakel AT, Elias, M and Barnett, JC 1982, Collier, W.A.: Geological Survey of Western Australia, 1:250 000 Geological Series Explanatory Notes, 29p.

Cawood, PA and Tyler, IM 2004, Assembling and reactivating the Proterozoic Capricorn Orogen: lithotectonic elements, orogenies, and significance: Precambrian Research, v. 128, p. 201–218.

Collins, PLF and McDonald, IR 1994, A Proterozoic sediment-hosted polymetallic epithermal deposit at Abra in the Jillawarra sub-basin of the central Bangemall Basin, Western Australia: Geological Society of Australia; 12th Australian Geological Convention, Perth, Western Australia, 1994, Proceedings; Abstract Series, no. 37, p. 68–69.

Cooper, RW, Langford, RL and Pirajno, F 1998, Mineral occurrences and exploration potential of the Bangemall Basin: Geological Survey of Western Australia, Report 64, 42p.

Fisher, RV and Schmincke, H-U 1984, Pyroclastic Rocks: Berlin, Springer-Verlag, 472p.

Fletcher, IR, McNaughton, NJ, Aleinikoff, JA, Rasmussen, B and Kamo, SL 2004, Improved calibration procedures and new standards for U–Pb and Th–Pb dating of Phanerozoic xenotime by ion microprobe: Chemical Geology, v. 209, p. 295–314.

Fletcher, IR, Rasmussen, B and McNaughton, NJ 2000, SHRIMP U–Pb geochronology of authigenic xenotime and its potential for dating sedimentary basins: Australian Journal of Earth Sciences, v. 47, p. 845–860.

Fletcher, IR, McNaughton, NJ, Davis, WJ and Rasmussen, B 2010, Matrix effects and calibration limitations in ion probe U–Pb and Th–Pb dating of monazite: Chemical Geology, v. 270, p. 31–44.

Foster, G, Kinny, P, Vance, D, Prince, C and Harris, N 2000, The significance of monazite U–Th–Pb age data in metamorphic assemblages: a combined study of monazite and garnet chronometry: Earth and Planetary Science Letters, v. 181, p. 327–340.

Gee, RD, de Laeter, JR and Drake, JR 1976, Geology and geochronology of altered rhyolite from the lower part of the Bangemall Group near Tangadee, Western Australia: Geological Survey of Western Australia, Annual Report 1975, p. 112–117.

Harrison MT, Catlos, EJ and Montel J-M 2002, U–Th–Pb dating of phosphate minerals, *in* Phosphates: Geochemical, Geobiological and Materials Importance *edited by* MJ Kohn, J Rakovan, and JM Hughes: Mineralogical Society of America, Reviews in Mineralogy and Geochemistry, vol. 48, p. 523–558.

Johnson, SP, Sheppard, S, Rasmussen, B, Muhling, JR, Fletcher, IR, Wingate, MTD, Kirkland, CL and Pirajno, F 2009, Meso- to Neoproterozoic reworking in the Gascoyne Complex and what it means for mineral exploration: Geological Survey of Western Australia, Record 2009/2, p. 23–25.

Ludwig, KR 2008, Isoplot 3.6: A Geochronological Toolkit for Microsoft *Excel*: Berkeley Geochronology Center, Berkeley, California, Special Publication 4.

Ludwig, KR 2009, SQUID-2: a user's manual: Berkeley Geochronology Center, Berkeley, California, 100p.

Martin, DMcB 2004, Peperite in the Backdoor Formation and its significance to the age and tectonic evolution of the Bangemall Supergroup: Geological Survey of Western Australia, Annual Review 2002–03, p. 53–59.

Martin, DMcB and Thorne, AM 2000, Another Jillawarra-style sub-basin in the Bangemall Supergroup — implications for mineral prospectivity: Geological Survey of Western Australia, Annual Review 1999–2000, p. 31–35.

Martin, DMcB and Thorne, AM 2004, Tectonic setting and basin evolution of the Bangemall Supergroup in the northwestern Capricorn Orogen: Precambrian Research, v. 128, p. 385–409.

Martin, DMcB, Sheppard, S and Thorne, AM 2005, Geology of the Maroonah, Ullawarra, Capricorn, Mangaroon, Edmund, and Elliott Creek 1:100 000 sheets: Geological Survey of Western Australia, 1:100 000 Geological Series Explanatory Notes, 65p.

Martin, DMcB, Sheppard, S, Thorne, AM, Farrell, TR and Groenewald, PB 2007, Proterozoic geology of the western Capricorn Orogeny — a field guide: Geological Survey of Western Australia, Record 2006/18, 43p.

Martin, DMcB, Sircombe, KN, Thorne, AM, Cawood, PA and Nemchin, AA 2008, Provenance history of the Bangemall Supergroup and implications for the Mesoproterozoic paleogeography of the West Australian Craton: Precambrian Research, v. 166, p. 93–110.

Morris, PA and Pirajno, F 2005, Mesoproterozoic sill complexes in the Bangemall Supergroup, Western Australia: geology, geochemistry and mineralization potential: Geological Survey of Western Australia, Report 99, 75p.

Muhling, PC and Brakel, AT 1985, Geology of the Bangemall Group — the evolution of an intracratonic Proterozoic basin: Geological Survey of Western Australia, Bulletin 128, 266p.

Nelson, DR 1995a, 91591: porphyritic rhyolite, Tangadee; Geochronology Record 85: Geological Survey of Western Australia, 4p.

Nelson, DR 1995b, 112107: granodiorite, Jillawarra sub-basin; Geochronology Record 85: Geological Survey of Western Australia, 4p.

Occhipinti, SA 2007, Neoproterozoic reworking in the Paleoproterozoic Capricon Orogen: evidence from $^{40}Ar/^{39}Ar$ ages: Geological Survey of Western Australia, Record 2007/10, 41p.

Occhipinti, SA and Myers, JS 1999, Geology of the Moorarie 1:100 000 sheet: Geological Survey of Western Australia, 1:100 000 Geological Series Explanatory Notes, 20p.

Occhipinti, SA, Sheppard, S, Myers, JS, Tyler, IM and Nelson, DR 2001, Archaean and Palaeoproterozoic geology of the Narryer Terrane (Yilgarn Craton) and the southern Gascoyne Complex (Capricorn Orogen), Western Australia — a field guide: Geological Survey of Western Australia, Record 2001/8, 70p.

Pirajno, FM, Hell A, Thorne, AM and Cutten HN 2009, The Abra deposit: a breccia pipe polymetallic mineral system in the Edmund Basin, Capricorn Orogen: implications for mineral exploration: Geological Survey of Western Australia, Record 2009/2, p. 31–33.

Rasmussen, B, Fletcher, IR and McNaughton, NJ 2001, Dating low-grade metamorphic events by SHRIMP U–Pb analysis of monazite in shales: Geology, v. 29, p. 963–966.

Rasmussen, B, Fletcher, IR and Sheppard, S 2005, Isotopic dating of the migration of a low-grade metamorphic front during orogenesis: Geology, v. 33, p. 773–776.

Rasmussen, B, Fletcher, IR, Muhling, JR, Thorne, WS and Broadbent, GC 2007a, Prolonged history of episodic fluid flow in giant hematite ore bodies: Evidence from in situ U–Pb geochronology of hydrothermal xenotime: Earth and Planetary Science Letters, v. 258, p. 249–259.

Rasmussen B, Fletcher IR, Muhling JR, Mueller AG and Hall GC 2007b, Bushveld-aged fluid flow, peak metamorphism and gold mobilization in the Witwatersrand basin, South Africa: Constraints from in situ SHRIMP U–Pb dating of monazite and xenotime: Geology, v. 35, p. 931–934.

Sambridge, MS and Compston, W 1994, Mixture modeling of multi-component data sets with application to ion-probe zircon ages: Earth and Planetary Science Letters, v. 128, p. 373–390.

Sheppard, S 2004, Unravelling the complexity of the Gascoyne Complex: Geological Survey of Western Australia, Record 2004/5, p. 26–28.

Sheppard, S, Occhipinti, SA and Nelson, DR 2005, Intracontinental reworking in the Capricorn Orogen, Western Australia: the 1680–1620 Ma Mangaroon Orogeny: Australian Journal of Earth Sciences, v. 52, p. 443–460.

Sheppard, S, Farrell, TR, Bodorkos, S, Hollingsworth, D, Tyler, IM and Pirajno, F 2006, Late Paleoproterozoic (1680–1620 Ma) sedimentation, magmatism and tectonism in the Capricorn Orogen: Geological Survey of Western Australia, Record 2006/3, p. 11–12.

Sheppard, S, Rasmussen, B, Muhling, JR, Farrell TR and Fletcher IR 2007, Grenvillian-aged orogenesis in the Palaeoproterozoic Gascoyne Complex, Western Australia: 1030–950 Ma reworking of the Proterozoic Capricorn Orogen: Journal of Metamorphic Geology, v. 25, p. 477–494.

Smithies, RH, Howard, HM, Evins, PM, Kirkland, CL and Wingate, MTD 2009, New insights into the geological evolution of the west Musgrave Complex: Geological Survey of Western Australia, Record 2008/19, 25p.

Stacey, JS and Kramers, JD 1975, Approximation of terrestrial lead isotope evolution by a two-stage model: Earth and Planetary Science Letters, v. 26, p. 207–221.

Thorne, AM and Martin, DMcB 2007, Peedawarra, W.A. Sheet 2349: Geological Survey of Western Australia, 1:100 000 Geological Series.

Thorne, AM, Cutten, HN, Hell, A and Pirajno, F 2009, Kiangi Creek Formation paleogeography and the geological setting of the Abra polymetallic deposit: Geological Survey of Western Australia, Record 2009/2, p. 29–30.

Tornos, F 2006, Environment of formation and styles of volcanogenic massive sulphides: the Iberian Pyrite Belt: Ore Geology Reviews, v. 28, p. 259–307.

Tornos, F and Heinrich, CA 2007, Shale basins, sulphur-deficient ore brines and the formation of exhalative base metal deposits: Chemical Geology, v. 247, p. 195–207.

Vogt, JH 1995, Geology of the Jillawarra area, Bangemall Basin, Western Australia: Geological Survey of Western Australia, Report 40, 107p.

Vogt, JH and Stumpfl, EF 1987, Abra: a stratabound Pb–Cu–Ba mineralisation in the Bangemall Basin, Western Australia: Economic Geology, v. 82, p. 805–825.

Williams, IS 1998, U–Th–Pb geochronology by ion microprobe, *in* Applications of Microanalytical Techniques to Understanding Mineralizing Processes *edited by* MA McKibben, WC Shanks, and WI Riley: Reviews of Economic Geology, v. 7, p. 1–35.

Wingate, MTD 2002, Age and palaeomagnetism of dolerite sills intruded into the Bangemall Supergroup on the Edmund 1:250 000 map sheet, Western Australia: Geological Survey of Western Australia, Record 2002/4, 48p.

Wingate, MTD, Pirajno, F and Morris, PA 2004, Warakurna large igneous province: A new Mesoproterozoic large igneous province in west-central Australia: Geology, v. 32, p. 105–108.

Wingate, MTD and Kirkland, CL 2009, Introduction to geochronology information released in 2009: Geological Survey of Western Australia, 5p.

Wingate, MTD, Kirkland, CL, Sheppard, S and Johnson, SP 2010, 185945: pegmatite lenses in metamonzogranite, Yinnetharra Homestead; Geochronology Record 901: Geological Survey of Western Australia, 5p.

Wingate, MTD, Kirkland CL and Thorne, AM in prep., 149031: felsic volcaniclastic rock, Boundary Bore; Geochronology Record 871: Geological Survey of Western Australia.

RECORD 2010/12

IN SITU U–PB MONAZITE AND XENOTIME GEOCHRONOLOGY OF THE ABRA POLYMETALLIC DEPOSIT AND ASSOCIATED SEDIMENTARY AND VOLCANIC ROCKS, BANGEMALL SUPERGROUP, WESTERN AUSTRALIA

RASMUSSEN ET AL.

This Record is published in digital format (PDF) and is available online at <www.dmp.wa.gov.au/GSWApublications>.
Laser-printed copies can be ordered from the Information Centre for the cost of printing and binding.

Further details of geological products produced by the Geological Survey of Western Australia can be obtained by contacting:

Information Centre
Department of Mines and Petroleum
100 Plain Street
EAST PERTH WESTERN AUSTRALIA 6004
Phone: (08) 9222 3459 Fax: (08) 9222 3444
www.dmp.wa.gov.au/GSWApublications